ANALYSIS AND DESIGN OF A HYPER-ELLIPTICAL CAMBERED SPAN MORPHING AIRCRAFT WING

A Thesis

Presented to the Faculty of the Graduate School

of Cornell University

in Partial Fulfillment of the Requirements for the Degree of

Master of Science

by

Justin Edward Manzo

August 2006

ABSTRACT

Morphing aircraft are a focus today due to their ability to combine multiple mission flexibility with a single vehicle. The Hyper-Elliptical Cambered Span (HECS) wing is one such wing being developed as a testbed for morphing technologies, due to its ability to vary the spanwise curvature in order to alter a craft's lift-to-drag performance. Through analysis of the aft-swept wing geometry and review of theory, predictions of aerodynamic performance are benchmarked against quasi-static rigid wing models in the Cornell University low-speed wind tunnel facility. Models assume a discretized approximation of the continuously varying spanwise curvature, with system order reduced significantly via a spool-and-tendon mechanism linking motions proportionally. The traditional rib-and-skeleton framework is replaced by a composite structure more adept at withstanding compressive loads due to actuation as verified through finite element analysis. Actuation methods are contrasted between a DC motor driven system and one employing shape memory alloy (SMA) wires, which generate proportional motion by linking sections electrically rather than mechanically. An energy comparison reveals the SMA wire to be more efficient, resulting in a prototype with embedded SMA wire actuators. The prototype employs a nonlinear proportional-integral controller to reach desired wing setpoints, which can be modified to user specifications based on flight conditions. A thermomechanical system model for the SMA is detailed and implemented in the feedback law, which relates well to observed actuation. The prototype half-wing is dynamically tested over a range of angle of attack in the wind tunnel facility. Results confirm the hypothesis that the planar wing will perform better than an elliptical wing of comparable characteristics, while morphing to the 'furled' state further increases lift-to-drag only over a small range of angle of attack. The SMA mechanism is demonstrated to be a viable means of morphing the wing, capable of overcoming aerodynamic loads and holding a desired wing shape based on the feedback law. Metrics of success are delineated and future revisions and inclusions are discussed.

BIOGRAPHICAL SKETCH

Justin Manzo graduated from Cornell University in 2003 with a Bachelor's of Science in Mechanical Engineering and a concentration in dynamics and control. He has worked extensively on robotic systems in the past, with an understanding of mechanical design, microcontroller implementation, structural modeling, and aerodynamic theory and experimentation principles. He was featured on Animal Planet's *Chasing Nature*, a show regarding graduate engineers and their research on animal behavior replication. Work to date has focused on implementation of alternative actuators such as shape memory alloys with applications to both terrestrial locomotion and aerial shape change mechanisms. Current projects include bat- and avian-inspired wing morphing mechanisms as well as insect-like walking mechanisms.

ACKNOWLEDGEMENTS

I would like to acknowledge NASA Langley and the Graduate Student Research Program, fellowship grant number NGT-1-03021. I would also like to thank my advisors at NASA Langley, Dr. Garnett C. Horner and Dr. Lucas Horta, as well as my advisor at Cornell, Dr. Ephrahim Garcia, without whom none of this would be possible.

TABLE OF CONTENTS

LIST OF FIGURES

LIST OF TABLES

LIST OF SYMBOLS

b	Wingspan
b'	Morphed wingspan
c	Chord length
C_D	Drag coefficient
C_{Di}	Induced drag coefficient
C_L	Lift coefficient
E	Young's modulus
I_{in}	Motor current
J_a	Polar moment of inertia of armature
J_L	Polar moment of inertia of load on motor
K	Burkett's induced drag factor
k	Cone's efficiency factor
k_e	Back-EMF constant
k_t	Motor torque constant
L	Motor inductance
$M_{X,i}$	torque on section i about X-axis.
q	Downwash velocity (from Cone)
R	Motor resistance
r_{ik}	Radius of spool from spool k-1 to spool k
r_k	Radius of spool from proximal spool k to distal moment arm
$r_{max,\,k}$	Half maximum chord thickness at joint k
r_{sk}	Radius of spool from proximal spool k to distal spool $k+1$
T	temperature
T_f	Friction torque
T_L	Aerodynamic torque exerted on motor
V	Airspeed

V_{in}	Voltage input
w	Downwash velocity (from Weissinger)
$\bar{x}, \bar{y}$	Coordinates along the ¼-chord line of the wing
α	Angle of attack
β	Spanwise camber factor
Γ	Circulation
ε	Strain
θ	Wing twist angle
$\theta_{rel,k}$	Relative angle change between sections *k* and *k+1*
$\theta_{\beta i}$	furled reference angle for joint *i*
$\theta_{\gamma i}$	planar reference angle for joint *i*
μ	Morphing parameter
μ_{GR}	Granda's wing metric, wing loading/wing weight
η	Nondimensional spanwise coordinate
ξ	Phase fraction of martensite
σ	SMA stress
ψ	Span ratio factor
Ω	phase stress tensor

Chapter 1: Introduction

1.1 Background

Throughout the history of conventional aircraft design, the majority of aircraft have each fulfilled one primary goal. In order to maximize efficiency, vehicles were developed with particular cruise configurations and fixed wings with minimal amounts of 'morphing' devices. These morphing elements consisted of components that allowed the wing or frame to change shape to alter performance, such as the F-14 and Tupolev Blackjack wing sweep mechanisms (Day, 2006), or even devices as prevalent as flaps and slats, which can affect camber, improve boundary layer energy, and extend wing chord to avoid stall by increasing lift while minimizing drag during take-off and landing (Shevell, 1983). However, aircraft remained predominantly single-mission vehicles, with the occasional addition of mechanisms to allow for a broader range of operating points.

The goal of NASA Langley's morphing program is to expand the capabilities of a single craft for multiple-mission flexibility. As new technologies have become available to the designer, conventional aircraft design can be rethought, and wings can become adaptable to the point where one particular craft may be able to optimize not just over a range of speeds, but an entire range of flight characteristics. Wings can be designed to twist and warp similar to the Wright brothers flyer of 1905, or to stretch and compress, in order to form a craft that can be optimized as both a long-loiter surveillance-style vehicle and as a high maneuverability or fast-dash one. Work by Sanders et al has begun investigating these 'smart' aerospace structures in attempts to reduce the size of military aircraft fleets (Sanders et al, 2004).

1.2 HECS Wing

The Hyper-Elliptical Cambered Span (HECS) wing was designed by Dr. Barry Lazos at NASA Langley (Davidson et al, 2003). Dr. Lazos' paper describes a design which

morphs an aft-swept tapered wing with the planform profile of a hyperellipse – an ellipsoid with power greater than 2 - into an anhedral of separate hyperelliptical profile in the Y-Z plane (Lazos, 2005). The profile for the wing furl is:

$$\left(\frac{z+4.727}{4.727}\right)^{2.5}+\left(\frac{y}{13}\right)^{2.5}=1 \tag{1}$$

where x is in the streamwise direction, y along the span, and z pointing downwards, as defined in Figure 1. The planform curves for the planar wing are:

$$\left(\frac{9.522-x}{9.522}\right)^{2.5}+\left(\frac{y}{15.121}\right)^{2.5}=1,\ \left(\frac{4.727-x}{4.727}\right)^{2.5}+\left(\frac{y}{15.121}\right)^{2.5}=1 \tag{2}$$

for the leading edge and trailing edge planform curves respectively. The wing can conform to any shape along the prescribed path between the flat, or 'planar' state, and the fully morphed, or 'furled', state. The HECS wing, in the planar state, provides a 15 percent increase in lift-to-drag ratio over a planar elliptical wing with an increase in surface area of only 10 percent, with expanded capabilities as the wing morphs to the furled state.

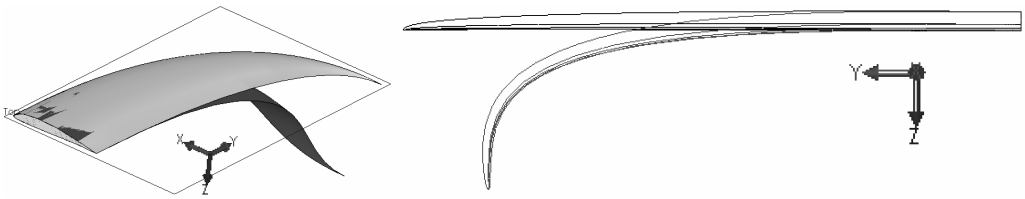

Figure 1: Planar and furled HECS wing shapes, isometric (at left) and frontal projection (at right) views showing hyperellipse curves in X-Y and Y-Z planes

When furled, the tips act as modified winglets, limiting vortex roll-up from the lower to upper surface of the wing, and further increasing lift-to-drag ratio over a certain range of angle of attack. What would ultimately be revealed was that for low α, L/D decreases for the furled wing, but for high α, the furled wing performs better. Because of the ability to drastically change aerodynamic performance in conjunction with a novel means of geometry adjustment, the HECS wing was selected as a testbed for physical implementation. The goal of this research is to analyze mechanisms for use on the HECS

wing and to verify performance benefits of the HECS wing over conventional wings through a combination of analytical and experimental testing.

1.3 Potential Challenges

The theoretical shape of the HECS wing is defined by a continuous curve in three dimensions, which poses serious challenges in terms of mimicking conventional wing design. Traditionally, a framework of ribs and spars is used to carry the transverse shear loading developed in flight, which is optimized for minimal weight and space. However, any proposed mechanism changing the shape of the wings in the Y-Z plane must account for the addition of rotational torques on many of the internal components if a mechanism were to be housed within the wing, and for the presence of compressive loading within the wings were a mechanism to actuate from within the fuselage, a force not commonly encountered in traditional craft. This compressive loading arises to be of chief importance, as the wing weight should be kept low to avoid vibration problems, while also maintaining minimal complexity in the small volume of the wing interior. As a consequence, though a rigid frame of the planar HECS wing can be constructed with relative ease in the conventional manner, alternative structural techniques must be employed to create a morphable wing.

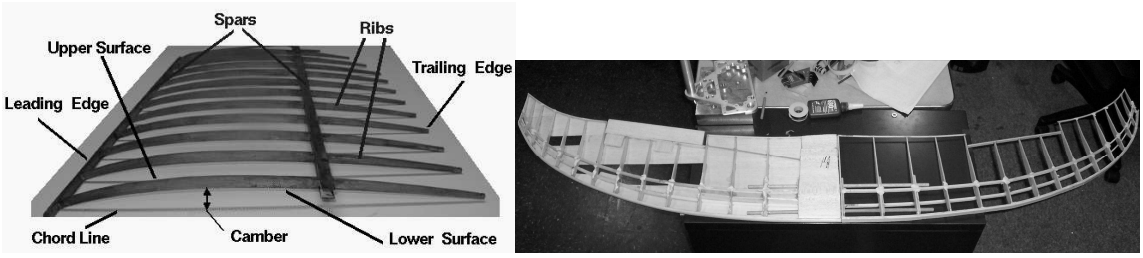

Figure 2: Wright Brothers' wing skeleton (left) with fixed-frame structure. Rigid HECS wing (right) modeled on this shape

With current technology, a continuously variable morphed shape would be impractical to build, though its aerodynamic merits due to the elimination of induced drag around sharp edges would certainly be worthy of an attempt. However, as a first-cut design, a discrete

approximation of the spanwise curvature is used. In addition, the design would benefit from reduction of the morphing maneuver to as few degrees of freedom as possible. Even though the shift from planar to furled shape is a complex ellipsoid in two dimensions, the curvature follows a prescribed trajectory which can be tracked by a single degree of freedom if a carefully designed mechanism could be developed. This would allow for minimal system complexity, especially important in a structure that would have to be revised and strengthened from the more conventional airframe skeletons of the past century.

The HECS wing will be benchmarked against the claims stated in initial design papers, requiring wind tunnel testing comparing it to an elliptical wing of comparable airfoil shape. In addition, it will be designed to fly on a testbed aircraft, meaning the mechanisms will have to be practical in their weight and power restrictions. Because of this, the scale of the wing is set to match the planform area of a 60" span square wing model R/C trainer aircraft, giving it a span of 72.4" to match the 698 in^2 area of the trainer wing in question. In this way, a half-wing can be fabricated for testing in the Cornell University 3'x4' low-speed wind tunnel facility, and a second half can later be constructed to add directly onto a flying prototype.

Chapter 2: Aerodynamics

2.1 Theory

The HECS wing is based on theoretical works dating back as far as 1962. Research on nonplanar lifting systems and their relation to lift and induced drag indicated the potential for nonplanar elliptical wing shapes to increase the effective aspect ratio of a wing (Cone, 1962). This was done by controlling the spreading vortex wakes that were shed off the trailing edge of the wings, which create an effective downwash at a point P due to a vortex line of strength dΓ at point P' after integration along the arc *s*:

$$\left(q_{\Sigma}^{P}\right)_{eff} = \frac{1}{4\pi}\int_{s}\frac{1}{r}\cos\left(\tau-\theta\right)_{P}\frac{d\Gamma}{ds}ds\,, \tag{3}$$

with conventions listed below.

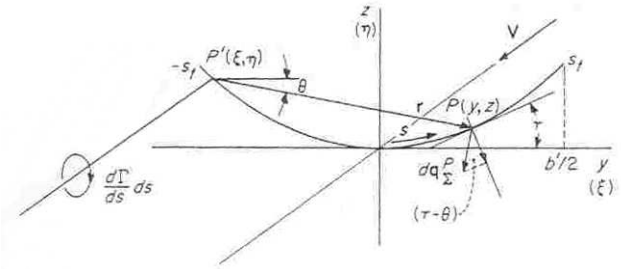

Figure 3: Force and velocity relations for an arbitrary lifting arc lying on the Y-Z plane.

The conditions for minimizing this downwash are satisfied by spreading out the lifting elements over a large area, demonstrated by the effectiveness of biplanes and endplates. Cone goes on to define an effective aspect ratio $A_{eff} = kA$ that takes into account an efficiency factor *k*, ultimately relating back to the induced drag in the form

$$C_{Di} = \frac{C_L^2}{\pi A_{eff}}. \tag{4}$$

Generally speaking, *k* is a constant as long as an optimum circulation distribution exists on the nonplanar wing:

$$k = \frac{1}{\psi^2 \pi} \frac{\left(\frac{\Gamma_0}{w_0}\right)}{\left(\frac{b'}{2}\right)} \int_{-1}^{1} \frac{\Gamma}{\Gamma_0} d\gamma, \tag{5}$$

though Cone goes on to solve analytically for *k* for various parabola, specifically circular arc segments and complete ellipses. Equation 3 is reduced to a function of wing geometry for these cases:

$$k = \frac{(1.00 + f(\beta))}{\psi^2} \tag{6}$$

where β is a spanwise camber factor defined as

$$\beta = \frac{d}{b'/2} \tag{7}$$

and has a similar effect on the experimentally derived correlations between *k* and β as it does on the analytical expression of equation 4.

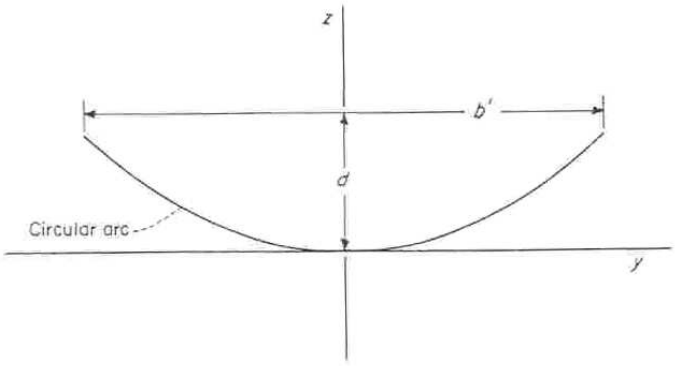

Figure 4: Convention for camber factor of spanwise curved wing sections

For other wing shapes, an analogy was made to electric potentials, and semielliptical arcs were tested experimentally using a conducting sheet, various arc shapes, and voltage probes. The resulting figure indicates the variation of the efficiency factor, which can be used to find the reduction in induced drag given that the span ratio factor ψ is unity, a claim made repeatedly in the paper. Estimating the hyperelliptical spanwise shape change as a simple elliptical arc segment, the reduction in induced drag using Cone's formula for β =.2987 and *k* =1.18 is estimated at 15.3% given that ψ=1.

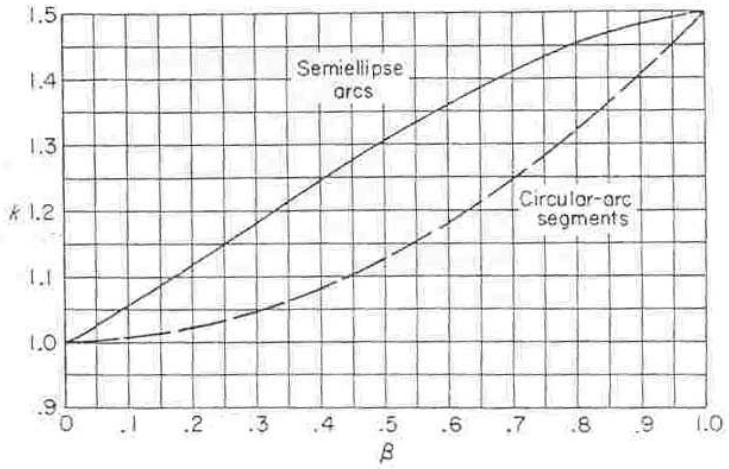

Figure 5: Variation of efficiency factor *k* of semiellipse arcs with camber factor, ψ=1.0

The factor $\psi = b/b'$, however, complicates the equation in all cases, entering in as a correction factor for cases where ψ is non-unity, implying that the span has changed as a consequence of the morph. The HECS mechanism was designed to keep a constant arc length during the shape change, and not to keep the span constant, such that $\psi \neq 1$. The correction enters into the equation in the inverse for analytical expressions, as seen in eq. 4. In order to determine the true induced drag change, the span ratio for the HECS wing morph of ψ=1.163 must be taken into account, yielding not the 15.3% drag reduction but conversely an increase of 14.6%. This failure to reduce the induced drag indicates a flaw in morphing to a nonplanar state without also stretching the wing, which was never mentioned by Lazos et al as part of the HECS wing morphing maneuver. Still, the Cone paper reveals that the general effect of the HECS wing morph is to effectively create endplates, only with a distributed spanwise curvature towards a vertically-oriented tip rather than one vertical member at the tip. Were the wing to stretch as well as bend, it could potentially offer great benefits to the lift-to-drag ratio while in the morphed state, though at least an approximation of the expected results could now be hypothesized. Cone's work was focused on the nonplanar wing shape into which to morph along the span, while the planform shape was influenced more by biology than geometry. Burkett

(1989) drew inspiration from evolution by investigating the success of shore birds such as the albatross and the swift, each with aft-swept wingtips and somewhat of a crescent shape. His work revisited Prandtl's established equation for induced drag (equation 2), which is minimized for an elliptical wing shape. The theory is based on modeling the wake shed off the wing as a flat trailing vortex sheet, which is not what would be produced by a swept wing. Therefore, derivations showing the elliptical wing as the most optimized shape are not necessarily the only means of finding a highly efficient wing shape, if the assumption of the flat vortex sheet is rejected. The paper describes the ability of a swept wing to generate a nonplanar vortex arc, dependent on α, that is pointed downwards at the tips, comparable to the physical shape of Cone's proposed wing shapes. The planar crescent wing, in particular, sheds a vortex wake that is semi-elliptical in nature, allowing for induced drag reductions of up to 5% by the time one reaches $\alpha=12^{o}$. The best vortex arc for a low induced drag factor $K=C_{Di}/(C_{Di})_{ell}$ to be a wing with aft-pointing tips at 90^{o} from a straight wing, representative of a wing having endplates. However, as this induces substantial flow separations, the crescent shape develops the lowest K before morphing to a nonplanar shape.

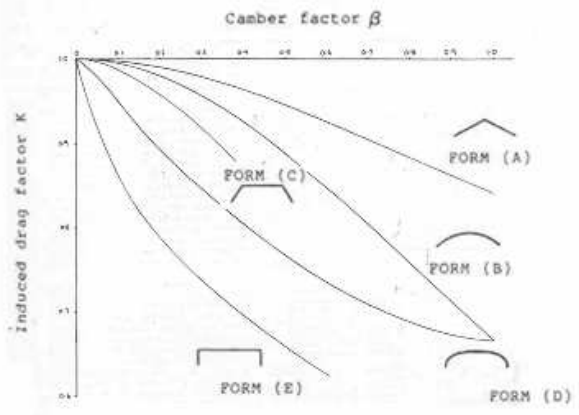

Figure 6: Variation of minimum induced drag factor with camber factor of vortex arcs for various arc forms induced by planar wing shapes, form 'D' induced by planar, crescent wing shapes

Van Dam (1987) uses a surface panel method for testing various wings held at a constant aspect ratio and concludes that a crescent-shaped wing will have 8.0% less induced drag than an elliptical wing of the same span and lift, validating these claims.

In total, it can be concluded that the HECS wing was designed to model the crescent-like albatross wings in the planar state, and then morph the tips downwards to incorporate further expected merits of altering the vortex wake. Though the wake for the HECS wing would have followed an approximate elliptical arc claimed by Burkett to yield a low induced drag factor, the wing morph does not incorporate the projected span change required by Cone for maintaining further induced drag reductions as a function of morphing into the furled state from simply having a hyperelliptical, planar wing. Therefore, the following predictions could be made:

a) that a planar hyperelliptical wing would exhibit improvement over an elliptical wing of the same aspect ratio, most likely on the order of 5%-10% increase in lift-to-drag ratio, and
b) that the changed from the planar to the furled state during morphing will yield a decrease in lift-to-drag on the order of 15%, based on the corrections for span change in conjunction with tip deflection.

2.2 Analytical and Computational Methods

The theoretical merits of the HECS wing being understood, computational methods could be employed to determine more accurately the expected aerodynamic properties of the wing. In this way, expected spanwise lift and drag profiles could be determined for calculating the mechanism loading, as well as use in calculating stability derivatives for trim analysis to determine flight-worthiness. Due to the complexity in the three-dimensional geometry of the wing, computational fluid dynamics-based methods were not practical, so calculations were made using much faster methods in MATLAB.

2.2.1 Analytical Approach

As a first attempt to determine the mechanism loading, a simple technique was used to measure the approximate lift on the planar HECS wing, before complex methods would need to be employed to figure out the forces involved in morphing. Schrenk's approximation for nonelliptical spanwise load distributions was used as a rough-cut method for determining the lift on the wing, assuming that the gaps present in using discrete segments were to be ignored (Manzo et al, 2004). The method states that any untwisted planar wing's spanwise load distribution shape can be approximated by the average of its actual planform shape and an elliptic wing shape of the same span and area (Schrenk, 1940). The desired total lift for the expected craft can be found, and the averaged profile can be used to determine the distribution of this lift over the HECS wing surface when in the planar state. However, the problem with this approximation is that it is not valid for swept wings, where vortex flow behaves differently along the wing as the trailing vortices no longer form a flat sheet, as mentioned earlier. The forces felt at the wingtips for these swept wings are expected to be higher than predicted, and computational methods must be employed (Raymer, 1999). Still, as a point of departure, the approximation could be used to predict a general range of loading for the planar wing, whereas the furled spanwise lift distribution would have to be determined experimentally due to the complexity of the vortex wake and the induced drag reduction it yields.

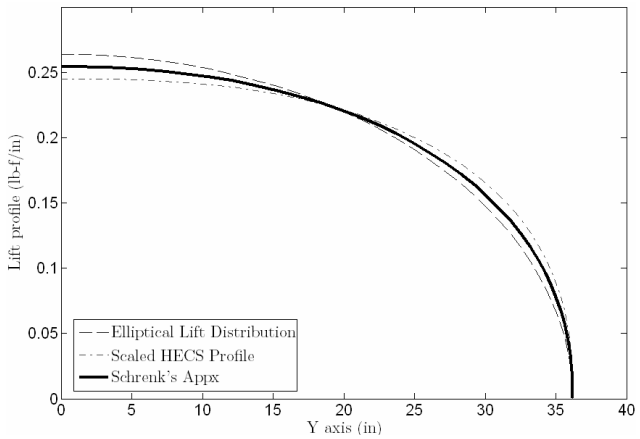

Figure 7: Schrenk's Approximation of Lift Profile for Planar HECS Wing

Raymer also mentions that for a wing with dihedral, the vertical lift component can be found simply by dividing by the cosine of the dihedral angle. For the discrete wing sections to be used on the HECS wing, this simple method is effective in calculating lift while in the morphed state, as each section is rotated purely in the Y-Z plane relative to neighboring sections. However, when tendon loading is considered, the torque generated at each joint is not purely dependent on the lift, but instead on the forces perpendicular to the wing surface, reflecting the planar lift forces. The purely planar Schrenk's approximation, then, was used to develop a set of forces to be acting on each joint of the wing, noting that it was not entirely valid due to the effects of vorticity at the tips. The results indicated a torque on the root section of 117.85 in-lb necessary to overcome 15 pounds total lift (7.5 lb per wing), and 22.55 in-lb at the tip of the first section necessary to rotate the second.

2.2.2 Weissinger Method of Computational Analysis

At this time, research was completed on a new computational method for calculating the lift and drag on any planar wing, including swept wing profiles. Adam Wickenheiser, who works at Cornell's Laboratory for Intelligent Machine Systems (LIMS) on analytical methods for determining morphing flight characteristics, developed an algorithm employing a modified version of the Weissinger method (Wickenheiser et al). This method determines lift and drag profiles based on the circulation around and downwash off the wing, in accordance with Prandtl's lifting line theory. In the original work, the paper defines two methods for calculating spanwise lift and drag based on the circulation at a finite number of panels (lifting surface, or "F" method) or airfoils (lifting line, or "L" method) (Weissinger, 1947). The lifting line approach is computationally simpler, and as it agreed with experiments and an earlier Multhopp approximation for swept wing parameter distributions (Multhopp, 1938), it was selected as a basis for Wickenheiser's revisions. Weissinger's "L" method assumes that the downwash on the wing, which has

contributions from the vorticity induced by the lifting line and the vorticity of the trailing wake, is dependent on circulation about the lifting line approximated at the ¼-chord point. By the Pistolesi-Weissinger condition, the effective angle of attack (α+ twist angle, both known quantities) at the ¾-chord line is equal and opposite to the downwash angle at this location (Pistolesi, 1937). If the circulation can be found, the downwash angle at the ¼-chord point can be determined at each station, which can be used to determine overall lift and drag.

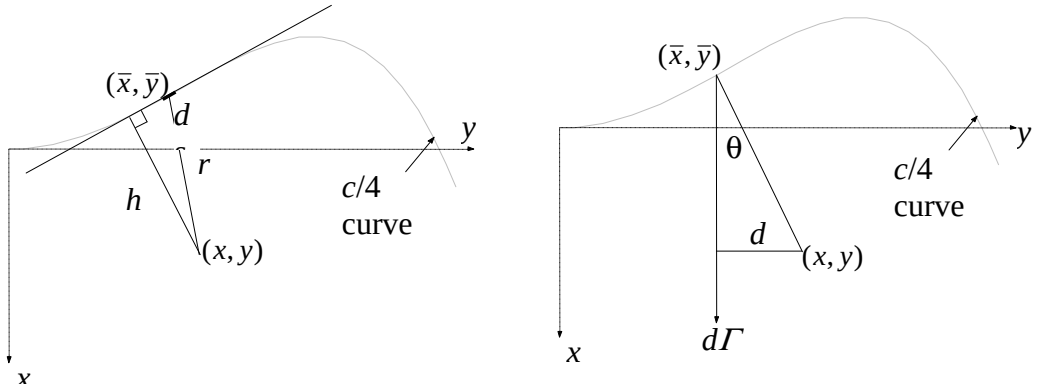

Figure 8: Downwash contribution from a lifting arc showing coordinate representations in the plane of the wing (x,y) and along the 1/4-chord line $(\bar{x},\bar{y})$

The constitutive equation states that for a general point (x,y) in the plane of the vortex sheet, the "L" model has induced downwash velocity

$$w(x,y)=\frac{1}{4\pi}\int_{-b/2}^{b/2}\frac{1}{y-\eta}\left[1+\frac{1}{x}\sqrt{x^2+(y-\eta)^2}\right]\Gamma'(\eta)d\eta\,, \tag{8}$$

where η is the nondimensional spanwise coordinate in the plane of the wing. The contribution from the lifting line is:

$$dw(x,y)=\Gamma(\bar{y})\frac{\left[x-\bar{x}(\bar{y})+\bar{x}'(\bar{y})(\bar{y}-y)\right]d\bar{y}}{4\pi\left[(x-\bar{x}(\bar{y}))^2+(y-\bar{y})^2\right]^{3/2}},\ \text{where}\ \bar{x}'(\bar{y})=\left.\frac{d\bar{x}(y)}{dy}\right|_{y=\bar{y}} \tag{9}$$

and the downwash contribution from an infinitesimal vortex element dΓ in the trailing vortex sheet is:

$$dw(x,y)=\frac{\Gamma'(\bar{y})}{4\pi(y-\bar{y})}\left(\frac{x-\bar{x}(\bar{y})}{\sqrt{(x-\bar{x}(\bar{y}))^2+(y-\bar{y})^2}}+1\right)d\bar{y} \tag{10}$$

Rearranging and incorporating the effects of the downwash from vorticity in the trailing vortex sheet yields:

$$\begin{aligned} w(x,y)=&\frac{1}{4\pi}\int_{-b/2}^{b/2}\frac{\Gamma'(\bar{y})}{y-\bar{y}}d\bar{y}+\frac{1}{4\pi}\int_{-b/2}^{b/2}\frac{\Gamma'(\bar{y})}{y-\bar{y}}\frac{x-\bar{x}(\bar{y})}{\sqrt{(x-\bar{x}(\bar{y}))^2+(y-\bar{y})^2}}d\bar{y}\\ &+\frac{1}{4\pi}\int_{-b/2}^{b/2}\Gamma(\bar{y})\frac{x-\bar{x}(\bar{y})+\bar{x}'(\bar{y})(\bar{y}-y)}{\left[(x-\bar{x}(\bar{y}))^2+(y-\bar{y})^2\right]^{3/2}}d\bar{y} \end{aligned}, \tag{11}$$

which can be evaluated for the downwash condition at the ¾-chord line based on the Pistolesi-Weissinger condition after removing singularities, yielding

$$\begin{aligned} w(y)=&\frac{1}{2\pi}\int_{-y_0}^{y_0}\frac{\Gamma'(\bar{y})}{y-\bar{y}}d\bar{y}+\frac{1}{4\pi}\int_{-y_0}^{y_0}\frac{\Gamma'(\bar{y})}{y-\bar{y}}\left[\frac{\bar{x}(y)-\bar{x}(\bar{y})+c(y)/2}{\sqrt{(\bar{x}(y)-\bar{x}(\bar{y})+c(y)/2)^2+(y-\bar{y})^2}}-1\right]d\bar{y}\\ &+\frac{1}{4\pi}\int_{-y_0}^{y_0}\Gamma(\bar{y})\frac{\bar{x}(y)-\bar{x}(\bar{y})+c(y)/2+\bar{x}'(\bar{y})(\bar{y}-y)}{\left[(\bar{x}(y)-\bar{x}(\bar{y})+c(y)/2)^2+(y-\bar{y})^2\right]^{3/2}}d\bar{y} \end{aligned}. \tag{12}$$

The formula is then nondimensionalized in length and velocity to obtain an expression for α as a function of the circulation $G=\Gamma/U_\infty$, which is omitted for conciseness. The circulation about the wing is then found by approximation as a nondimensional sine series representation with *m* terms:

$$G(\phi)=\sum_{k=1}^{m}a_k\sin(k\phi),\ \text{where}\ a_k=\frac{2}{\pi}\int_0^{\pi}G(\phi)\sin(k\phi)d\phi\ \ \text{and}\ \ \phi\equiv\cos^{-1}(\bar{\eta}) \tag{13}$$

To solve for a_k, Multhopp's formula uses a Gaussian quadrature to reduce the integral to the summation

$$a_k=\frac{2}{m+1}\sum_{n=1}^{m}G(\phi_n)\sin(k\phi_n),\ \text{where}\ \phi_n=\frac{n\pi}{m+1}. \tag{14}$$

This set of circulation terms is related back to the angle of attack at each station to solve a system of *m* equations with *m* unknowns, and given this Γ, the downwash can be

determined an infinite distance behind the wing. Munk's analysis states that the downwash at the ¼-chord line is equal to half of this quantity (Munk, 1921):

$$\frac{1}{2}\lim_{x\to\infty} w(x,y) = \frac{1}{4\pi}\int_{-y_0}^{y_0} \frac{\Gamma'(\bar{y})}{y-\bar{y}}\,d\bar{y}\,. \tag{15}$$

From here, the wind vector can be adjusted by rotating the lift and drag coefficient terms determined by 2-d airfoil theory to yield an adjusted set of spanwise coefficients, which are then integrated over the length to yield overall lift and drag on the wing.

Therefore, the process used in Wickenheiser's algorithm is as follows:

a) The wing is discretized into a number (*m*) of spanwise airfoil stations, to have results interpolated between them. This allows the complex three-dimensional wing shape (for the planar wing with airfoils of different size) to be reduced to a finite number of two-dimensional airfoils, with the resolution determining computation time and accuracy.

b) The nondimensionalized circulation at the quarter-chord point is expressed as a sine series of the form:

$$G(\phi) = a_1 \sin(\phi) + a_2 \sin(2\phi) + \ldots + a_m \sin(m\phi) \tag{16}$$

where there are *m* equations and *m* unknowns based on the downwash at the ¾-chord point. The system is solved simultaneously for all circulation terms.

c) Knowing the circulation, the downwash at infinity can be found by taking the integral of the vortex strengths, using the results from b). The downwash at the ¼-chord point is then half of the downwash an infinite distance behind the wing by Munk's analysis.

d) Two-dimensional airfoil theory is used based on a wing's true airfoil shape at each station's known α, θ, and downwash angle. This is integrated over the entire wing to find the net lift, drag, and center of pressure data, and can be plotted to find the spanwise distributions.

Because this method takes into account the effects of varying vortex strengths, it is highly effective in determining the aerodynamic properties of the planar HECS wing. It can be solved explicitly for straight wings only, but becomes a computational process with a numerical solution when the wings incorporate curvature that will alter the trailing vortex sheet. While not able to measure the performance for the furled wing shape, it can certainly be used to generate a much more realistic set of values for wing loading for the planar state, and consequently to determine the forces required in the tendons and required at the joints to maintain structural integrity.

It should be noted that this method still assumes a flat vortex sheet, but that the effects from the true vortex plane curvature are only significant very far behind the wing, whereas the circulation effects are calculated close to the wing using small angle approximations. Because of the fact that the Weissinger algorithm is a low-order method, the higher order terms that would contain the effects of this vorticity nonplanarity are not as significant. However, the nonplanar effects of the physically curved vortex plane are also minimal close to the wing, before they can roll off significantly in space rather than merely in intensity. The intensities of the vortex sheet near the wing are the relevant quantities used in calculations, a fact that is still incorporated in the method. Therefore, the algorithm takes into account some, but not all, of the effects of altering the vorticity of the wing from what is predicted for straight wings, making it an effective starting point for future analyses and experimentation on swept wings.

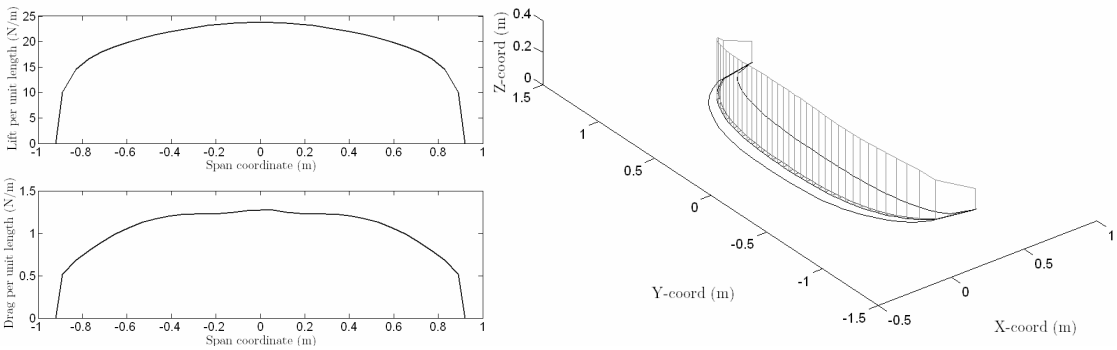

Figure 9: Spanwise planar HECS lift and drag distributions generated using Weissinger method (left), 3-d representation (right) for α=3.0^0, V=30 mph

The Weissinger method was used for the HECS wing geometry at the proper scale and at 30 mph airspeed, to generate the lift and drag profiles in addition to the coefficient curves. The results are smoother for lift, as drag involves higher order terms, yet they are more accurate than the earlier Schrenk's approximation based on their incorporation of vorticity effects, which predicts a required motor torque for contraction of 118 in-lb compared with a Weissinger prediction of 95 in-lb. Though the simulations are on the same order of magnitude, the Weissinger approximation is more accurate, having taken into account the effects of the swept tip. A three-dimensional load distribution is also shown for the HECS wing, indicating the relative scales of lift and drag for the cruise configuration of α=3^o at 30 mph.

2.3 Experimental Determination of Aerodynamic Properties

2.3.1 Formulation of Experiment

With a numerical solution to the planar HECS wing parameters already derived, a scientifically rigorous set of tests could be performed on rigid quasi-static wings to determine lift, drag, and moment coefficients with respect to α. Because the approximate solution for lift and drag can be found for a planar HECS wing and the Weissinger method can solve explicitly for an elliptical wing of a particular airfoil shape, two baseline wings exist that can be tested as control samples using the Cornell University 3'x4' low-speed wind tunnel. Once testing has been validated, the furled HECS wing,

which cannot be solved for numerically using either the Weissinger method or in a reasonable amount of time using CFD-based methods, can be tested to give lift and drag measurements. Therefore, a set of three wings would be sufficient for testing – an elliptical wing, a planar HECS wing, and a furled HECS wing, all of which using the HECS wing airfoil for consistency.

2.3.2 Test Apparatus

The data collection device adapted for use in the wind tunnel is JR3's six degree-of-freedom robotic load cell, connected to data acquisition software in MATLAB. The software interprets and decouples the three forces and three moments experienced by the load cell into lift, drag, and center of moment forces, and can take an input parameter file of α, airspeed, geometry, and environmental data to extract the coefficients. The load cell has mounted on it a low-profile sting to place the sample in the developed flow region of the tunnel, and can be modified to use either as a central sting or for use with a symmetry plane for half models. For initial testing, full wing models would be used.

In order to construct the wings, a Dimension Stratasys 3-d printing machine took geometry files and produced ABS plastic models of each of the wings. The wings held span and aspect ratio constant between elliptical and planar HECS, with a span of 32" and planform area of approximately 138 in^2 for both, for an aspect ratio of 7.4. The furled HECS wing was designed as the same initial span as the HECS wing, curved spanwise along the correct hyperellipse curve. The resulting models were then smoothed, filled, and mounted on the sting, as shown below.

Figure 10: Quasi-static wind tunnel model and setup

Tests were conducted at various speeds and over a plausible range of α for each wing, and the results were plotted alongside the expected values as well as experimental findings conducted at NASA LaRC. Results are shown averaged over a range of wind speeds for each α, and lift-to-drag is shown as a high-order polynomial curve fit when it appears more smooth than the data would suggest. While the results showed some discrepancy between experimental and computational/theoretical results, a number of conclusions could be drawn. The first plot is a comparison of elliptical and planar HECS wings, both experimentally reached and analytically derived. It shows that the planar HECS wing generates more lift over a wide range of α than the elliptical wing in the experimental runs, with comparable drag improvements. This was expected based on the theory predicted by Burkett for aft swept wingtips, but was not predicted by the analytical Weissinger simulations, which show that the elliptical wing should yield higher efficiency than the HECS wing shape. The results are an indication that the Weissinger simulation may not be entirely valid as a means of accounting for the non-planar trailing vortex sheet, which may be more significant to enhancing flight efficiency than can be accounted for with a simple lifting-line approach.

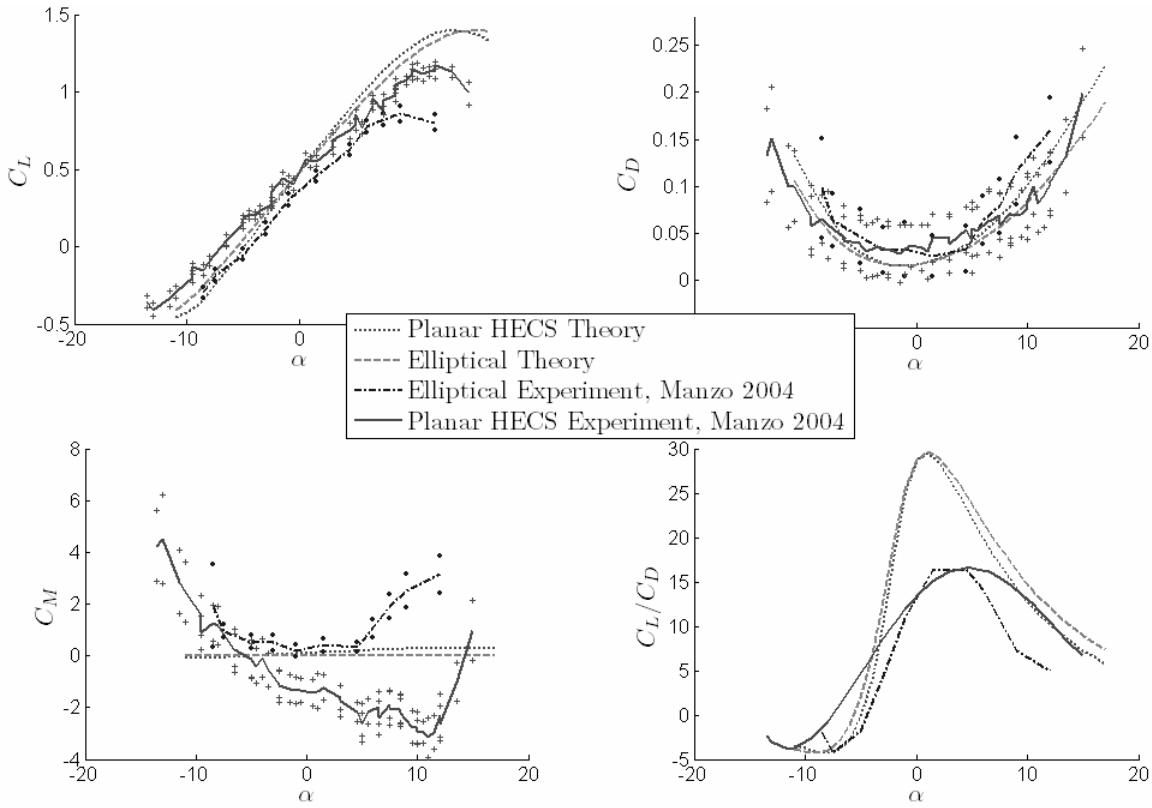

Figure 11: Planar HECS and elliptical profiles, analytical and experimental results

The next plot includes the furled HECS wing experimental results, as well as results found at NASA Langley. The furled HECS wing showed slight improvement over planar HECS performance only for a narrow range of α. Except for this particular flight regime where the furled wing demonstrates a higher lift-to-drag ratio than the planar HECS wing, these results correlate with the theory that a curved anhedral will only yield improvement if the span is held constant during morphing. However, comparing to the results found at NASA Langley (Lazos, 2004), the furled HECS wing may be more efficient than the experiments at Cornell were able to determine, based on the inherent turbulence of the tunnel facility and various experimental errors. One standard deviation of the lift, drag, and moment data is plotted for all Cornell experiments, showing the inconclusiveness of drag measurements in this flight regime.

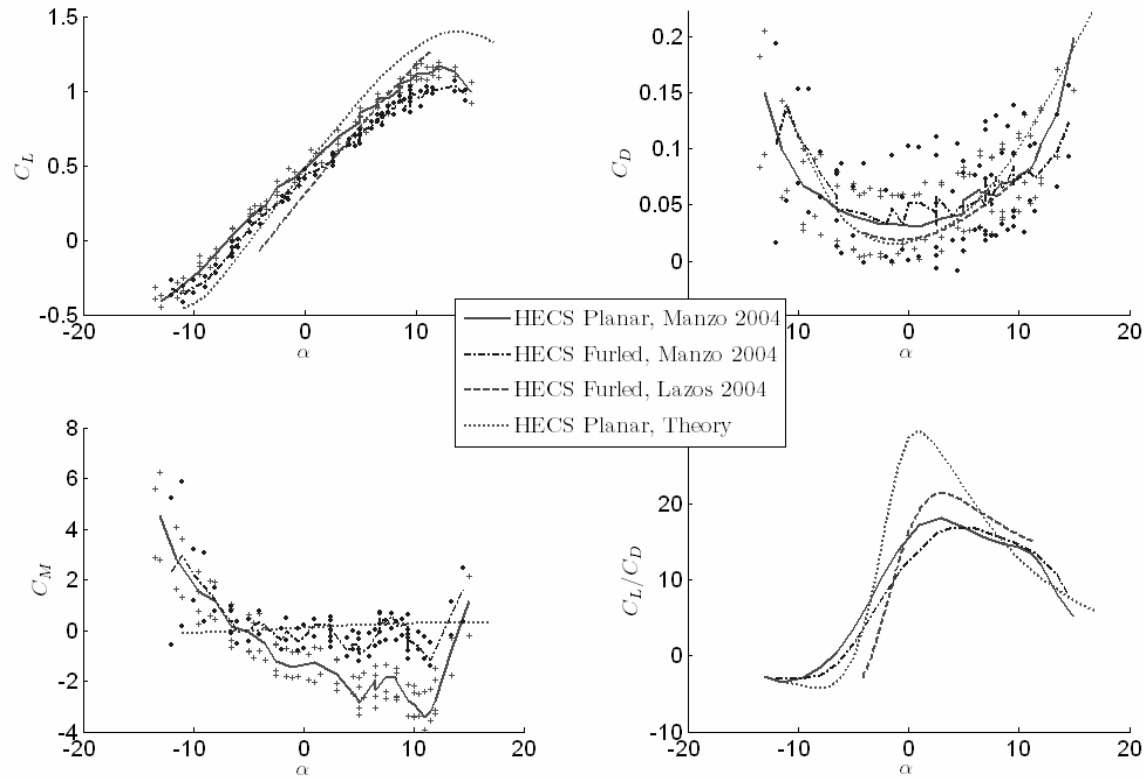

Figure 12: Selected aerodynamic profiles from 2004 quasi-static wind tunnel tests

From these test results, it is clear that the planar HECS wing performs well compared to an elliptical wing, though conclusions about the furled wing cannot be drawn confidently without further testing and more precise equipment. Dynamic test results will be used to test the effects of the furl maneuver and wing shape for high α, to determine if it does indeed increase flight efficiency in this regime.

Chapter 3 – Kinematic Investigations

3.1 Prior Work

Before attempting to build various wing components, kinematic mock-ups of various designs were investigated to test the theories of discrete approximations and reduction of system order. An ideal mechanism would be one that could control all segments of the wing with a single actuator housed in the fuselage. A number of mechanisms have been proposed for a morphing-style shape change. Some research has focused on variable geometry trusses to replace rigid members of the structure with bulky linear actuators, or using torque tubes to warp the structure based on the torsion developed in a cylinder subjected to compressive tendon loading. This can be either imprecise or excessively complex, as in the case of the "Trussarm" – a space manipulator arm that has in one version 99 degrees of freedom over a 15 meter span, with many redundant actuators to generate exactly specified shape changes (Hughes, 1991). Alternatively, tensegrity structures promise lower degree-of-freedom control for drastic shape change of a rigid lightweight framework of rods and tendons exclusively in tension, but are difficult to morph into specific shapes without altering other parts of the structure.

Other mechanisms have had success with direct manipulation of a plate or beam via tendons anchored at both ends, offset by a moment arm capable of generating a torsion component on the beam, and actuated by DC motors for both position and vibration control (Yoshida et al 1990, and Tani et al 1990). The systems were able to generate bending vibration suppression through a simple control scheme actuating the tendons to oppose the transverse waveforms generated by specific vibration modes, and could increase tendon force further to deform the beam into a particular shape. These tendon networks appeared the most promising systems for lightweight actuation with minimal

system complexity, capable of attaining a desired wing shape without complicating the overall geometry or adding a significant number of heavy actuators.

For integration into the HECS wing or comparable morphing wing, a novel single degree of freedom mechanism was developed by at Virginia Tech that uses a number of interdependent four-bar linkages to develop the correct shape change (Wiggins et al, 2004). This motion could be achieved with a single actuator, but carries high mechanism weight all the way out to the wingtips and requires many moving parts for actuation. At the University of Florida, a gull-wing morphing mechanism was designed using a linear actuator placed inside the fuselage of the 26" max. span wing and with a telescoping shaft with rigid links to actuate both joints of the wing (Abdulrahim & Lind, 2004). This provides a central actuator concept while still having protruding, weight-intensive wing mechanisms, and is a functional method of system order reduction with only minor drawbacks, including mechanisms interfering with flow around the wing.

3.2 Design Challenges

The ideal morphing mechanism for the HECS wing is one that minimizes component weight in the wings as well as system complexity. Various methods were considered, but one such mechanism met all requirements after wing shape approximations were made. This mechanism would actuate from within the fuselage with no elements protruding outside of the original wing, and promises simple actuation and mechanism design.

3.2.1 Single Degree-of-Freedom Concept

The most promising method for system order reduction came in the form of a network of coordinated tendons and spools 'tuned' to the motion of the morphing curvature. In this design, a motor housed in the fuselage would pull on tendons internal to the wing that would move distally towards the tips of the wings. This would be accomplished by a

number of varying radii spools along the span of the wing that would generate proportional motion changes according to the desired relative angle change between each section. In this way, each discrete section could be allowed to rotate a different amount from the others, though the ratios of change would be held constant. This allows for the exact trajectory of the morphing maneuver to be attained, as the change at every spanwise point along the wing is at the same percentage of the morph between planar and furled states. A schematic of this mechanism is shown below.

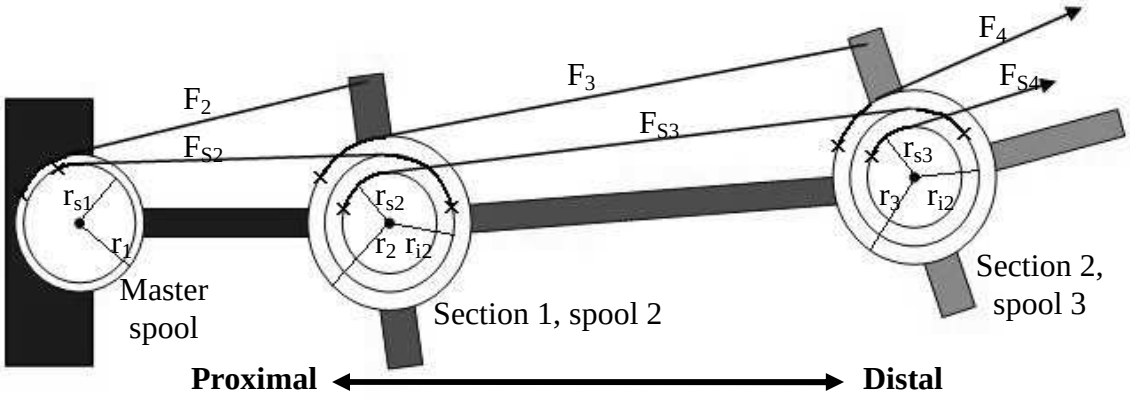

Figure 13: Schematic of single degree-of-freedom pulley mechanism

In this way, the complex morph between states has been reduced to a single parameter for use in calculations and controls, which actually expresses a complex three-dimensional change. This is useful in expressing aircraft performance as a function of a single morphing parameter, which can represent changes in camber, dihedral, and sweep with a single state variable.

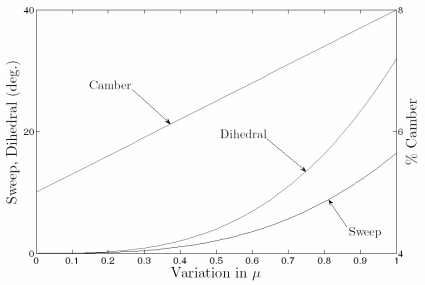

Figure 14: Complex geometry change represented by single morphing parameter, μ

This type of mechanism is not without precedent. Pulleys have become an integral part of modern engineering, and can be seen in devices such as elevators, cranes, and belt-driven machinery found in all modern automobiles. Sizing models have been developed based on stress and geometries that can be found in reference textbooks, along with a catalog of belt sizes and speeds (Avallone & Baumeister, 1996). One of the oldest chronicled examples of a pulley-based mechanism lie in Leonardo da Vinci's flapping wing mechanisms, as denoted in the Codex Atlanticus. The mechanism shown below, designed around 1494 in Milan, utilized rigid links to oscillate a reciprocating pulley system, which generated a prescribed flapping motion over a number of joints on a wing-like skeleton. The pulleys were used to reduce system order to a single set of actuators – the legs – in an attempt to reduce the highly complex avian flapping maneuver to a single degree of freedom. This highly polished representation of a human-powered flapping wing device was used to indicate the dynamic potential of the human body based on Leonardo's extensive avian studies as seen in his Codex 'On the Flight of Birds' (Taddei & Zanon, 2005).

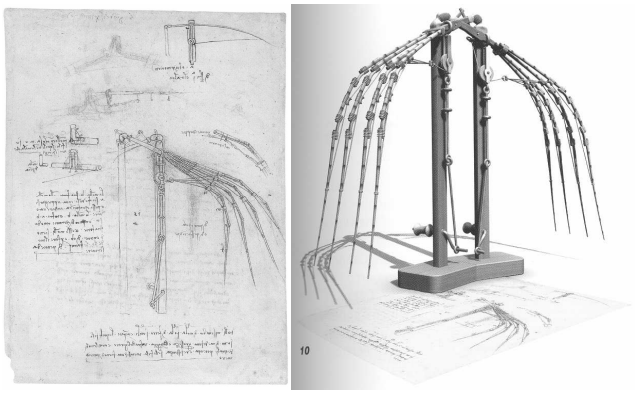

Figure 15: Leonardo's flapping wing mechanism, from the Codex Atlanticus. CAD rendering of machine by Taddei & Zanon, 2005

Another interesting example of a pulley mechanism credited to da Vinci (although more likely the work of his disciples and a combination of lesser concepts based on its reference in the Codex Huygens, a work pieced together years after da Vinci's death and potentially miscredited) were plans for the world's first automated humanoid robot.

Based on his studies on anatomy and kinesiology, the armored robot was designed to sit up, wave its arms, and move its head on a flexible neck while opening an anatomically correct jaw, perhaps to the accompaniment of automated drums (Florence Museum of the History of Science, 2006). Most interesting was the fact that all of this was accomplished with a connected network of pulleys and cables, controlled centrally in the chest. The robot had two independent systems - fully articulated four degree-of-freedom arms including joints at the shoulders, elbows, wrists, and hands, as well as three degree-of-freedom legs, ankles, knees, and hips. Because it is believed that the robot was designed for whole-arm grasping, arm movement was most likely coordinated to be done in unison. The legs were driven by a single crank to actuate all of the degrees of freedom simultaneously.

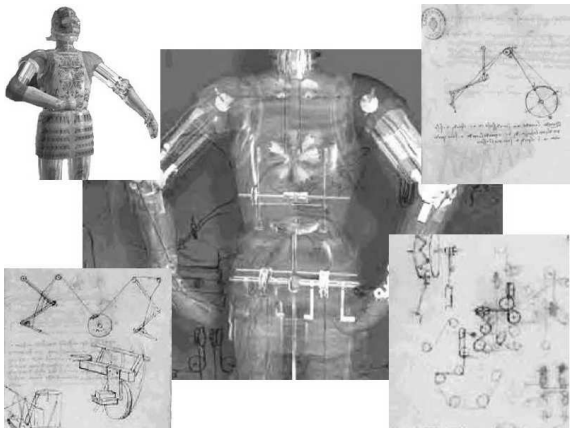

Figure 16: Leonardo Davinci's robot sketches, circa 1495. Renderings from Florence Institute and Museum of the History of Science

Leonardo's mechanisms are in many respects quite similar to the HECS wing mechanism. They can both be developed and tested easily, with only hinges, pulleys or spools, and tendons placed in the wings or appendages. They both hold promise for high complexity systems with single actuator control. With the proper spool sizing and ratios, all of the complex motions could be joined together by a centrally-located actuator. It therefore becomes the next task in developing the HECS mechanism to determine these ratios.

3.2.2 Curvature Approximation

It was decided that a finite set of discrete wing surfaces would be joined together to best approximate the curvature of the HECS wing, especially after the promise of the single degree-of-freedom spool and tendon design. Looking at the HECS wing furl in the Y-Z plane, it was decided that as a valid starting point, a five segment discrete wing could be fabricated to closely approximate the true HECS curvature. A least-squares fit in the Z-coordinates of the linear segments compared against the continuous curvature revealed the optimal locations to place discrete segments, shown below. The fit was based on the optimization

$$\min \sum \left(z_{appx}(y) - z_{true}(y) \right)^2 , \tag{17}$$

which is impacted most by tip discrepancy due to the increase in number of points along the original span once they are furled downwards.

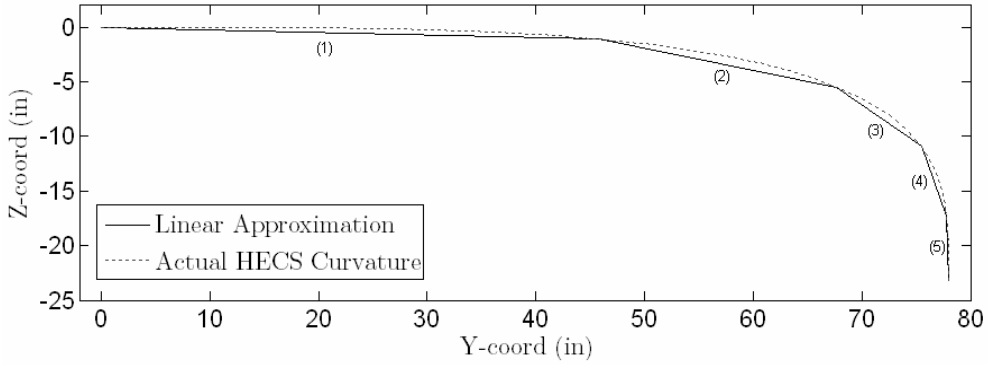

Figure 17: Discrete approximation of continuous spanwise HECS curvature

While this linearized curvature would clearly suffer some the penalty of increased drag due to the sharp edges, it would still allow for the macroscopic shape change, and could effectively demonstrate the validity of a mechanism such as that described above.

The mechanism used in the HECS wing is designed to be used antagonistically – that is, it can theoretically be actuated with a set of tendons to achieve the furled HECS shape,

and the shape can be reversed with a set of tendons acting opposite in direction to regain the planar HECS shape, similar to a bicep-tricep orientation. Therefore, any spools to be used as rotation points must be allowed to have similar moment arms about either direction of rotation in order to operate the morph in forward or reverse. To keep the mechanism entirely contained within the structure of the wing, and with the pivot centered in the thickest part of the chord, the moment arm of any tendon rotating a given wing section must be slightly less than half the max airfoil thickness, $r_{max,i}$. This data is known for the 5 locations at which pivots will be placed, and can be used to define the tendon forces.

Looking at the geometry of this shape change, the spool ratios can be easily calculated by looking at the relative angle change from one section to the next. For example, from joint (2) to joint (3), the angle change $\theta_{rel,3}$ is 23.63°. The traverse of the tendon is therefore $2\pi r_{max}\theta_{rel}/360^{o}$=0.149", where r_{max} is half of the maximum chord thickness at the joint. With the spool radius r_{s3} set at this value, and the input radius r_{i3} fixed at 0.3", the final radius r_3 can be found based on the desired traverse of section 4 based on the equality

$$r_3 = \frac{q_4 r_2 r_{i3}}{q_3 r_{s2}} = \frac{360 * 2\pi r_{\max,4}\theta_{rel,4} r_2 r_{i3}}{360 * 2\pi r_{\max,3}\theta_{rel,3} r_{s2}} = \frac{r_{\max,4}\theta_{rel,4} r_2 r_{i3}}{r_{s3}\theta_{rel,3} r_{s2}}, \tag{18}$$

with conventions as in Figure 11, and where all quantities are determined by wing geometry ($r_{max,4}$ and $\theta_{rel,i}$) and spool ratios more proximal to the wing. Effectively, as the rotation of the proximal spools with different radii contract the tendons, the radius needed for each distal spool is determined by the traverse needed along geometrically fixed radii. In this way, a network of components can be developed for kinematic testing.

3.3 Physical Design Evolution

In order to test the theory of proportional spools, a number of mechanisms were designed. The first was a generic aluminum model that did not take into account geometry or

loading, but employed the use of proportional spools with an actuator at the top and bottom of the root airfoil (for furl deployment and retraction).

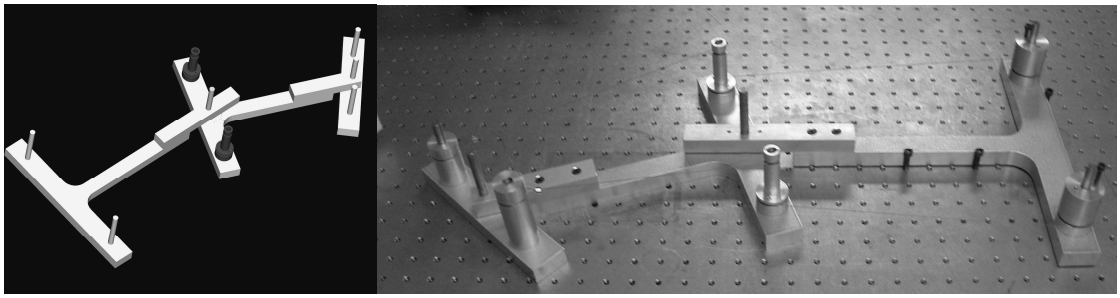

Figure 18: Rendering and model of initial sequential spool model

This mechanism demonstrated a flaw in that the system was underconstrained, and that unless tension was kept in the correct proportions on both the top and bottom set of tendons, the system would not automatically conform to the correct proportional motion change. There was no means of isolating θ_{rel} and θ_{spool}, as indicated in the accompanying schematic.

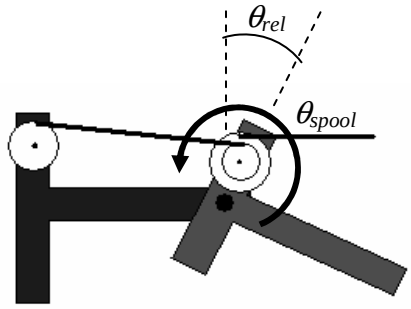

Figure 19: Underconstrained mechanism schematic

With only two different ratios on the spools, the proportional motion cannot be transmitted to the next rigid wing section independently from the spool at that section that is allowed to rotate independently, and the purpose of the mechanism is defeated.

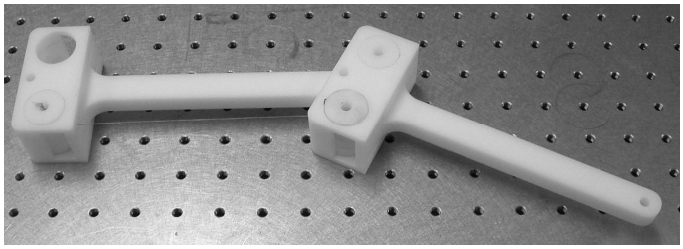

Figure 20: ABS plastic model of second-generation HECS kinematic mechanism

Subsequent design evolutions occurred predominantly in the form of ABS plastic models generated with a three-dimensional rapid prototyping machine, which generated accurate representations of varying ideas without necessarily being able to carry the true aerodynamic loading that would be experienced in flight. As the models were refined, two facts became obvious:

1) that each spool except the closest and furthest from the fuselage would necessarily have grooves for three different ratios, rather than two, and
2) that practical implementation of the idea given the potential loading and constrained spaces of the HECS wing airfoils may prove infeasible for this design.

The scaled components for a 72.4” wingspan, reflected in the accompanying CAD and prototyped mockups, illustrate the cramped space, and the final level of complexity for an antagonistic mechanism – a separate set of spools for contracting the wing to the furled state, as well as returning it to the planar shape. The scale on the largest rib mechanism (at the root) would be approximately 1” in max thickness, and for the smallest section would be represented by a rib of 0.45” max thickness for the furthest out section that would require components for morphing.

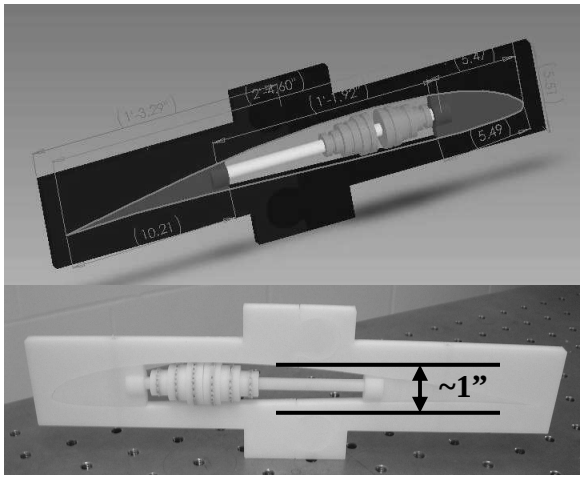

Figure 21: Rendering and model of scaled sequential spool model, indicating size and shape constraints

Given the space constraints, coupled with the loading in the tendons (discussed further in section 3.4), the assumption that a traditional rib and spar construction would offer insufficient compressive strength for this mechanism was tested. A wooden skeleton of balsa and basswood was constructed at scale, housing the mechanism for the largest three joint sections, which would also be carrying the largest loads. Upon actuation from the root, the structure failed, in particular through the main support spars in the root section. Placing upwards of 100 pounds of compressive force along basswood spars was not the intended structural loading of the conventional airframe, as the structure required strengthening to carry these loads. Further calculations are explained in section 3.4.1.

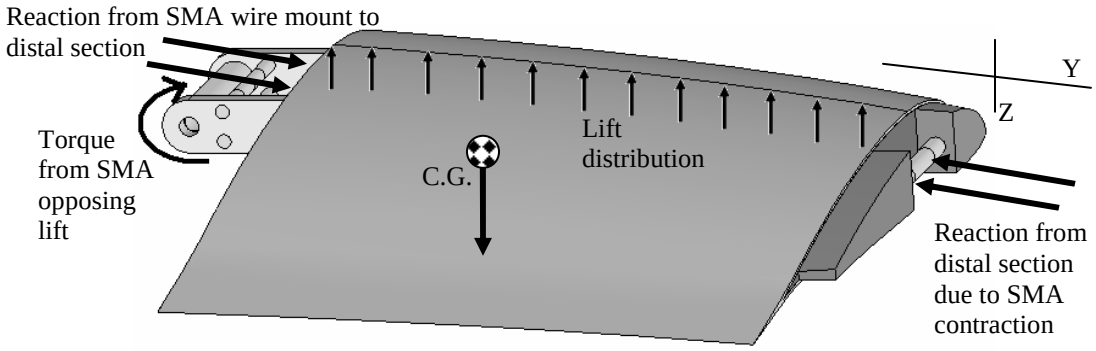

Figure 22: Free body diagram of principal Y-Z forces acting on representative section. Lift force is opposed by SMA wire bay to proximal section, removing spool moments, and compressive forces are generated by SMA wire to distal section.

Based on these results, another method of fabrication was considered that would be more capable of dealing with the compressive loading. A composite structure could be fabricated out of foam and fiberglass, which has the advantage of being strong in compression from the foam core and in tension from the fiberglass, to prevent the issues of buckling and compression failure found in the wood skeleton model. Fiberglass construction is common in ultralight glider designs, as well as in lightweight boat hulls and high-performance auto body frames. Typically the frames are made solely of cured fiberglass, but they can be reinforced with foam for further structural integrity.

According to sandwich theory, the flexural rigidity D, which is comparable for sandwich structures to the quantity *EI* for isotropic materials (Young's modulus times second moment of area, or the area moment of inertia):

$$D = E_f \frac{bt^3}{6} + E_f \frac{btd^2}{2} + E_C \frac{bc^3}{12}, \tag{19}$$

where E_f represents the modulus of the face material, E_c is that of the core, b is the width of the sandwich, t the face thickness, d the distance between center lines of faces, and c the core thickness (Allen, 1969). In this equation, the middle term dominates, and would yield a flexural rigidity of $2.43*10^4$ lb-in^2 for a rectangular cross-section approximation of the second section of the wing, compared against $3.11*10^4$ lb-in^2 for a the same section made of solid red northern oak in the weakest orientation to resist failure, or $3.88*10^5$ lb-in^2 in the strongest. The composite structure shows a weight loss of 77% compared to an equal volume solid wooden wing for comparable rigidity, which is comparable to the weight of balsa-based skeleton wing. If the fiberglass can be as rigid as a solid block of wood, it is unlikely that it will fail where a conventional rib-and-spar wing could not withstand the loading.

3.4 Physical Constraints

3.4.1 Loads

In order to generate the tendon loads on the HECS mechanism, aerodynamic data was applied to critical components. Running a Weissinger analytical analysis of the planar HECS wing, spanwise lift and drag forces for various angles of attack and windspeeds can be calculated. Choosing α=3 deg and V=30 mph, parameters which yield a net lift force of 8.3171 lb and drag of 0.4386 lb, allows for the generation of the two spanwise curves. These curves would not reflect the furled HECS lift and drag distributions, though they are assumed to fluctuate within 15% of the planar HECS values.

In order to measure the required resultant torques on the mechanism sections, the true HECS curve is discretized into 10 sections (5 for each wing half) that represent the discrete mechanism sections. The lift acting on all wing sections distally to a particular joint will contribute to the torque acting at that joint. The torque on each section for the right wing can be represented by

$$-M_{X_I} = \int_{a_I}^{b} L(y)(y-a)dy\,, \tag{20}$$

where $L(y)$ represents the lift force, and a_i and b are the spanwise joint and wingtip locations. In this way, the moment on the outermost section will integrate the forces and distances from the end of section 4 to the tip, whereas the root section will integrate the forces and distances from the root of the wing all the way out to the tip, as the root section will be absorbing the load of all sequential segments in the trim state.

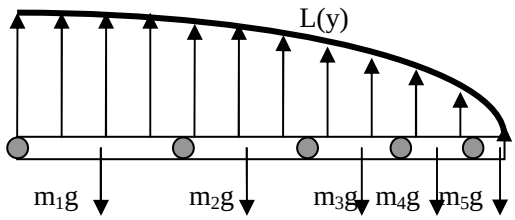

Figure 23: Free body diagram of right HECS wing with joints indicated

With this determined, the segment torques can be determined as a function of α and airspeed. It should be noted that these torques do not take into account the weight of the wing structures, which would create an opposing moment to the aerodynamic loads, and therefore decrease their net values.

Table 1: Torque, moment arm, and forces on each joint based on planar HECS analytical lift distribution

Section	T (in-lb)	$2r_{max}$ (in)	F (lbs)
1	67.583	0.95	142.28
2	13.865	0.877	31.634
3	2.849	0.723	7.8766
4	0.763	0.6	2.5423
5	0.114	0.453	0.5036

As seen in Table 1, the torques for a specific operating point drop off drastically from 68 in-lb on the proximal hinge to less than 0.5 in-lb at the most distal. Because of this, the mechanism will require significantly more support in the root sections than at the tips – a fact that is a strong detractor from attempting to integrate motion in the root section. This can be seen by analyzing the required forces necessary to generate such torque through the tendons.

While a standard rib-and-spar construction attached to the fuselage would be capable of supporting the root wing load and moment, transferring a single-point, 142 lb force on a single set of components is impractical. Given the 80 pound load capability of the 0.020" diameter Spectra line, a redundant tendon system would have to be implemented, which would in turn generate excessive torsional shear on the spools, high compressive loads on the structure, and unsupportable shear on any pins attaching the spools to the adjacent sections. For this reason, and the fact that joint 1 rotates 1.4^{o} nominally, the section most proximal of the five discrete wing parts will be constructed in such a way as to be fixed with respect to the fuselage, rather than rotating. This yields the following final mechanism shape profile, which was chosen to translate all other sections based on fixing the root rather than rotating each subsequent section to match the original HECS profile in space.

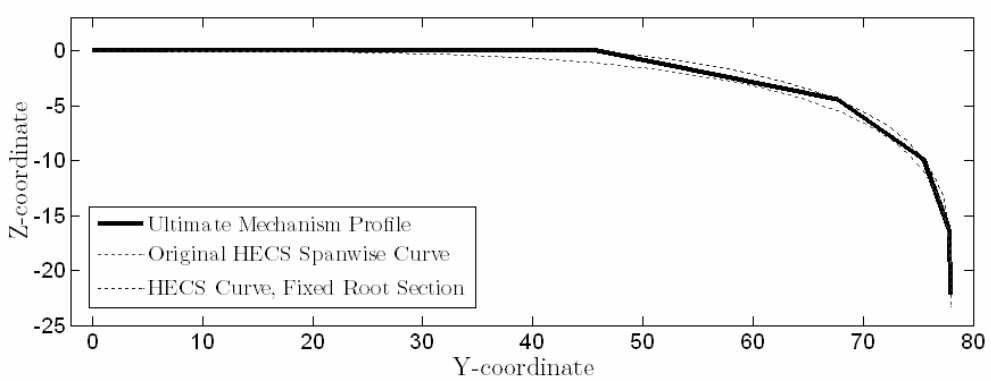

Figure 24: Final HECS morph shape showing discrepancy from true curve

This shape would still be effective at retaining the general HECS wing morphed profile, and will end up only with tip displacement discrepancies instead of gross relative angle errors, which should be inconsequential in terms of sensors used.

3.4.2 Materials Selection

With the morphing shape understood, and the loads calculated, two designs were available – the pulley-and-tendon model similar to the Da Vinci robot, and a direct wiring of shape memory alloy 'muscle wire' between sections with simple moment arms, depicted below. The SMA wiring would directly allow conversion of the tendon contraction into rotary motion, without the use of spools. This would employ the SMA directly as an actuator, whereas the pulley and tendon model requires a DC motor for actuation.

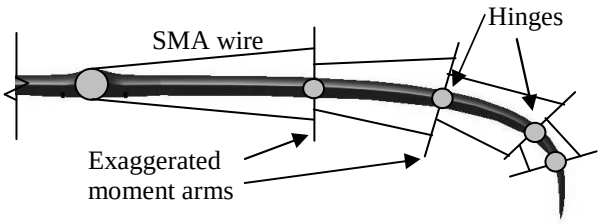

Figure 25: Simple moment arm schematic to employ SMA wiring

Additionally, the design employing passive tendons requires complex routing through the system in order to anchor the tendons and keep them in the correct kinematic ratios. As was seen in preliminary models, tendon alignment became a principal challenge. Due to the space constraints around the spool network, a tradeoff arose between a raised barrier preventing spool misalignment and achieving maximum moment arm length. Any relaxation of the tendons due to wing motion causes either misalignment or structural failure, which were indeed the two outcomes observed during testing. An SMA-actuated system would be more effective at keeping the system properly aligned, due to removal of the spools and separation of the tendons into shorter sections.

Since the traditional basswood skeleton failed during initial tests, a better means of carrying aerodynamic and compressive loading was needed. The use of composites proposed in section 3.2 would better reinforce the wing segments to prevent a failure due to the compressive loads generated by the tendons. The structural integrity of this system can be predicted by theory, but a more in-depth analysis is necessary to ensure that this wing construction can carry the loads with the minimum weight. This will be addressed in the next section.

The use of conventional skin materials for small-scale aircraft - specifically heat-shrink film that is intended for use over a rigid skeleton frame – will not function properly over the jointed sections of the wing, nor will it be necessary over the smooth epoxy finish of the composite. This indicates the need for small sections of a carefully chosen skin material over the gaps, to prevent drag concentrations at all joints due to openings and discontinuities. As a first-cut approach, latex skin with a pre-strain applied before actuation on both the upper and lower surfaces of each joint will hopefully alleviate the aforementioned problems expected during the morph. A second approach could be the incorporation of a ‘smart skin’ comprised of shape memory polymer, a thermally controlled viscoelastic polymer that retains rigidity and strain levels when below a threshold temperature. As with shape memory alloy, this polymeric film can be actuated to affect the state of the wing, with the difference being that the polymer will affect rigidity of the structure rather than physical orientation. Used in conjunction with the SMA wiring, however, this material can be used to create a mechanical locking device that will provide a rigid aerodynamic surface and also hold the wing in the proper morphed orientation without continuous energy consumption – an issue addressed in chapter 4.

3.4.3 Finite Element Analysis

In order to more accurately assess the ability of the composite-based airframe to carry the loads, a finite element model was generated in the Solidworks 2004 finite element package, COSMOS. This package allows for directly integrating loads and material properties into CAD representations, and can therefore measure the stresses and strains experienced under those loads. To predict the stress in the composite system, the second section was used as a representative model, as it carried a significant portion of the aerodynamic loads, and would be the section that carried both the largest and the most diverse compressive and tensile forces experienced due to tendon loading. These loads would act in tension at the root of the section as the large proximal bay pulled on the moment arm to generate rotation, and in compression in the core as the distal bay connecting it to further sections would contract during actuation.

The implemented constraints allowed for the structure to rotate about the pivot joints at the proximal edge, where a tendon bay would distribute an even pressure along the entire spool to be used as a moment arm. The pressure would be resolved such that it was a representation of the tendon loads measured in section 3.3.1, though the SMA wire was not the principal structural element under investigation. It was given an artificially high modulus of elasticity in order to model the system as being fixed at a cut plane in the SMA wire bay, and allowed to rotate about the pivot joint. In addition, a similar tendon bay would act at the distal edge, and would be resolved as forces acting around a hinged axis mounted to this face.

In applying the aerodynamic loads, the approximate distributions of lift and drag calculated analytically by the Weissinger method would be implemented at the quarter-chord line on the underside of the wing and at the leading edge, respectively. As COSMOS only accepts second-order polynomial pressure distributions projected along

two-dimensional planes onto three-dimensional surfaces, the spanwise lift and drag distributions were simplified to fit the input structure. The distribution was never calculated for the three-dimensional case but rather along the span, so this data was implemented as a one-dimensional second-order polynomial curve fit entered over a 1" wide strip along the quarter-chord line, as shown below. The simplification that these loads acted along three-dimensional lines, rather than over the entire surface of the wing, was used for three reasons: it was necessary given the limitations of the program, it was as accurate as theory could predict without knowing the full distribution of lift over the entire surface of the wing, and it was not as critical in the simulation as the effect of the compressive loads from the SMA onto the structure, which initially motivated the study.

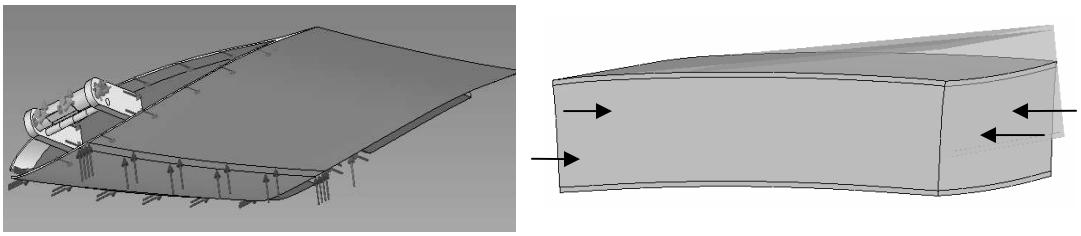

Figure 26: Load distributions used in FEA model. Red arrows denote pressure, purple forces, and green boundary conditions. Potential buckling mode shape due to compression, undeformed shape overlaid

The materials chosen for the model, and those used in the final implementation, were polyisocyanurate foam (commonly used in building insulation), E-glass fiberglass with an assumed post-cure thickness, ABS plastic to be used for critical ribs housing sensor equipment, and wooden moment arm supports, modeled as northern red oak based on available information in the literature (Green et al, 1999). All of these materials had known physical and structural properties, specifically Poisson's ratio, density, yield strength, and Young's modulus. All materials were assumed to be isotropic with the exception of the wood, which was assumed to be anisotropic instead of orthotropic due to limited capacities of the COSMOS software. The oak assumed the grain orientation that yielded the lowest factor of safety for tensile strength, as the wood was more likely to fail in tension than in compression.

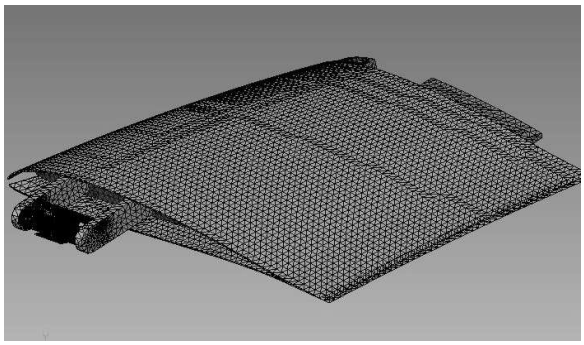

Figure 27: Mesh for HECS wing FEA analysis

The mesh was resolved into approximately 100,000 elements, with 163,055 nodes, and the simulation was run assuming flight conditions at approximately 30 mph, α=3^{o}. This would generate 0.959 lb lift and 0.051 lb drag on the wing section, and would require a net SMA pull force of 31.6 lbf to oppose the torque created by the lift forces. With the exception of the tendon material itself, which was not modeled due to material complexity, the structure was predominantly well below its acceptable yield stress limits. The only points of potential weakness lay along the moment arm that served as the anchor point for the SMA, which had a factor of safety for the von Mises stress of 1.8, or a stress of 4.518 ksi acting on the aluminum rods to be used.

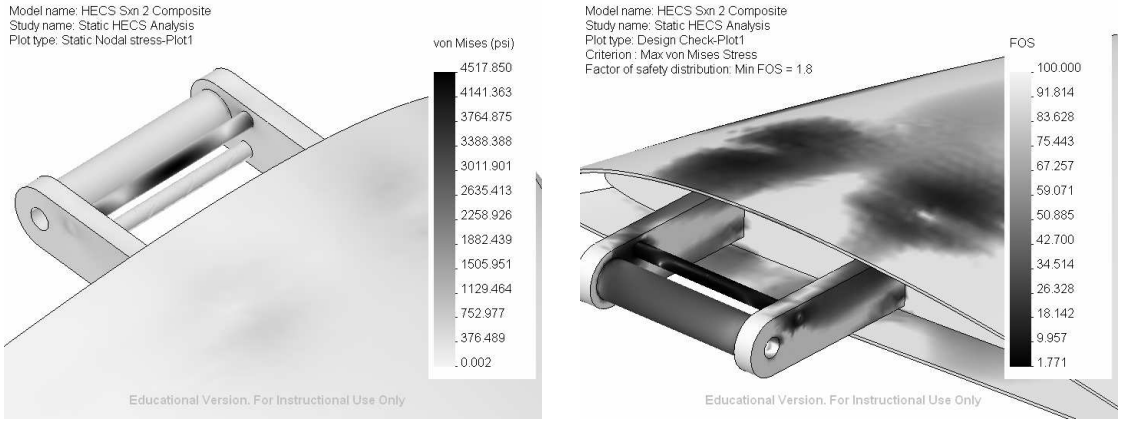

Figure 28: Predicted FEA von Mises stress and yield strength factor of safety results

As can be seen in the accompanying plots of factor of safety based on yield strength and the von Mises stress criterion and the von Mises stress plot, the only failure point would be not in the composite itself, but in the arms that would support the tendons, specifically in the aluminum rod and the wooden arms. Because of this, the solid wood was replaced

with a plywood laminate, which accepts higher stresses before failure, and the aluminum was replaced with hardened steel bolts. With this revision, the simulated structure had a minimum factor of safety of approximately 17 before yielding occurs, indicating the viability of composite fabrication for the wing. A buckling of the structure was unlikely to occur, as the strength of the foam was sufficient to prevent deflection of the outer shell, or to separate the foam from the fiberglass during compression.

3.5 Actuator Selection

In order to actuate the system for the DC motor, a force of 31.6 lb is developed in the tendon that will rotate the mechanism from section 2 outwards, as it was decided to lock the root section. This would develop a torque of 63.2 in-lbf at the root of the wing after mounting on a 1" diameter central spool. In order to accomplish this, a representative gearmotor (Faulhaber, 2006) would weigh approximately 564 g, with a no-load speed of 8.83 rpm at the output shaft. Since the required rotation for this joint is 10^o, this would yield a complete morphing shape change within 1.5 seconds, which is sufficiently fast for a one-time operation.

A critical metric for actuator selection, however, is power consumption. Under investigation was not only the energy needed for a single actuation from a flat to a furled wing, but the energy required to sustain this wing shape afterwards. For weight reduction purposes, a motor without a braking system was selected, meaning that a constant power draw would be necessary to sustain a certain wing shape with a resistive aerodynamic load present. Using the standard second-order equations of motion for a DC motor:

$$\begin{aligned} V_{in} &= L\dot{I}_{in} + RI_{in} + k_e\dot{\theta}_{root} \\ k_t I_{in} &= \left(J_a + J_L\right)\ddot{\theta}_{root} + T_f + T_L \end{aligned}, \tag{21}$$

and using the quoted values for the selected motor with a 24 V power source and a mass moment of inertia J_L of 120 lb-in^2, a response for voltage and current draw, and

consequently power, can be derived. This can be integrated over time to find the net energy into the system. The results are below, and indicate that the morph to steady-state requires 64.24 J to settle to within 3% of the desired final angle, and 8.69 W afterwards to hold the wing in that position. Conversely, models of shape memory alloy showing a sinusoidal phase change under adequate heating can be used to plot a simple power curve given quoted heating currents for a known diameter and length of wire. Knowing the required length of wire for contraction and the required number of strands for adequate pull force plus a factor of safety for gust loads, a 12 strand bay of 0.015" diameter wire in 1.8" lengths, heated at 2.75 A with a fully charged 12 V power supply (14.4 V) would be more than capable of sending a pulse-width-modulated power signal until the correct temperature is reached, and then would pulse power at 1 A to sustain temperature and maintain force on the actuators. This entire process requires 62.68 J to reach the right contraction length, and 4.56 W afterwards to sustain the shape. The SMA-actuated system, therefore, was selected as being capable of generating a wing morph with lower energy cost as well as lower sustained power consumption required to hold the wing in shape without the assistance of a rigid skin or mechanical lock carrying the aerodynamic loads. The SMA system, therefore, promises to weigh less, to require a lower voltage input, and to provide less mechanical complexity than a DC-motor actuated system.

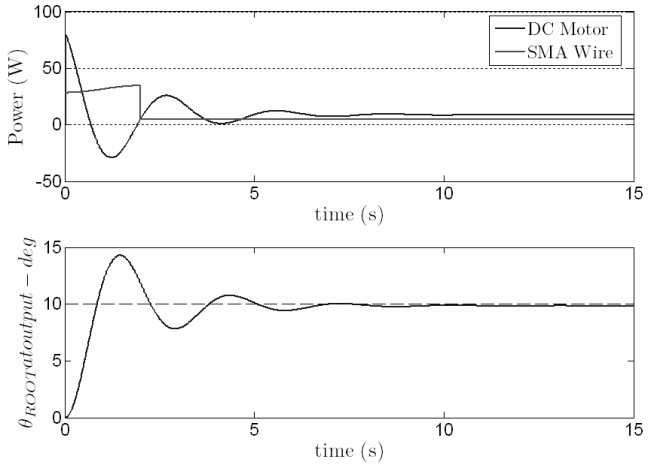

Figure 29: Energetics comparison for DC motor and SMA wire mechanism

3.6 Final Design

Based on the metrics for low weight and high strength with minimal energy usage, a composite structure was fabricated with SMA-based tendon actuators that were housed in the wing sections themselves, rather than a DC motor at the wing roots. The final prototype weighed 2.435 pounds and was comprised of four composite-based sections and a fifth ABS plastic prototyped section, based on complex geometry.

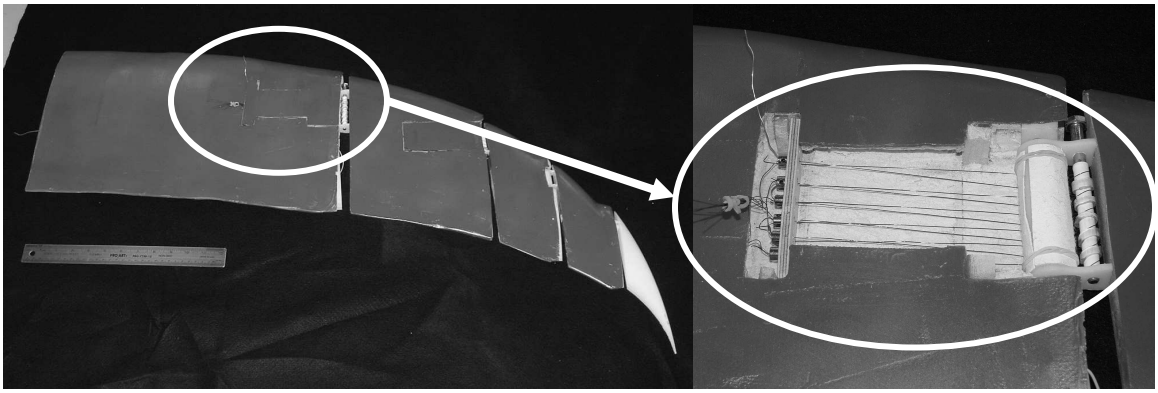

Figure 30: Final wing prototype, pre-skin

It was designed with attachment points to a sting through dowels inserted at the root, and with bays in the two root sections allowing SMA to be implemented at the required lengths for the desired actuation. As the length was slightly more than was required for the correct angular deflection at the SMA's specified contraction lengths, the controller would be responsible for allowing partial contraction by varying the transmitted power. The remaining two sections allowed the SMA to pass entirely through the section, as the span of each was approximately equal to the required length for the proper contraction distances.

Sensor equipment was embedded into the mechanism at the tips of each pivoting joint. The wooden ribs at the section tips were supplemented by prototyped plastic that contained ball bearings to reduce friction during rotation, as well as a rotary potentiometer coaxially located with the hinge rod. This rod, not shown, would be

rigidly attached to the potentiometer via the keyway in the sensor head, a key attached to the shaft, and a silicone coupling allowing expansion perpendicular to the axis of rotation to prevent damage to the sensor. In this way, the relative angles between segments could be directly measured by the voltage output of the four on-board sensors.

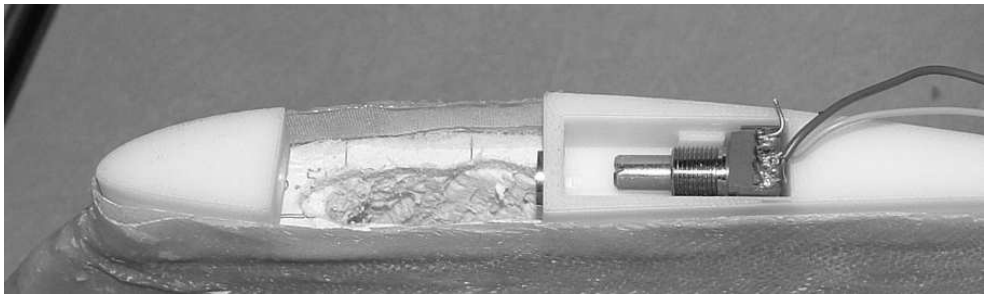

Figure 31: View of sensor and bearing placement

For the skin system, a combination of prestrained latex and 0.006" thick steel sheet metal were employed. This was an alternative to complex composites providing in-plane compliance and out-of-plane rigidity – the subject of future work. The thin metal sheaths were placed around the distal end of each section, and latex was adhered to this and to the root of the next section. In this way, the removable sheath could be separated from the wing and the skin could be temporarily loosened in order to make adjustments or repairs to the actuators. The latex was pre-strained such that it was taut regardless of wing shape, preventing as much flutter as possible. With this system in place, the net weight of the wing was 2.89 pounds, with 15.7% of the total wing weight consisting of this skin system. This is a significant increase, but tests without the skin showed that the wing generated insufficient lift to raise the hinged structure up to the flat state at 44 mph. The addition of the skin kept the wires between bays confined within the wing cross-section rather than protruding, as well as preventing some of the parasitic drag caused by the sharp edges between sections by acting as a fairing. The skin smoothed the general shape of the wing and prevented excess vortex shedding at each gap, lowering induced drag and consequently enhancing the lift as vortices could not expend energy by rolling up in the middle of the wing (Maughmer, 2002).

Chapter 4: System Control

4.1 Shape Memory Alloy Introduction

The final version of the morphed HECS wing employs shape memory alloy wiring. Specifically, Flexinol® wire, a nickel-titanium alloy fabricated by Dynalloy, is used in four independently controlled bays. As mentioned earlier, SMA is a thermally activated material that mimics human muscle. This is accomplished by allowing the material to transition between two crystalline states, according to various thermal characteristics. As can be seen on a temperature-time-transformation plot for steel, different states exist based on the rate of cooling and the temperature range of the material. As time progresses during the quenching process for very high temperatures, the metal will take various crystalline forms based on cooling rates.

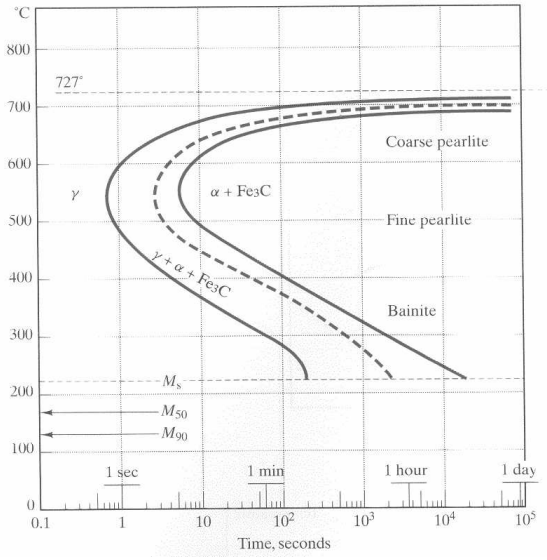

Figure 32: TTT diagram for steel (from Shackelford, 2000)

Given a certain annealed condition and under the correct stress conditions, shape memory wire will alternate between two of these states at a predictable and repeatable temperature (Hodgson & Brown, 2000). This temperature is determined by composition ratios and the microstructure as determined by the annealing process, and can vary from -190 ^{o}C to

200 ^{o}C. At temperatures above this transformation temperature (TTR), the SMA exists as an ordered cubic crystal form known as austenite. At temperatures below the transformation temperature (TTR), it exists as martensite, which has a monoclinic crystal structure with no right angles, resulting in alternating bands between layers that takes on a 'tilted' cubic or compressed form. In this form, the application of stress will result in flipping the direction of tilt, resulting in a 'detwinned' martensitic form that takes on additional strain values from the austenite/twinned martensite configurations.

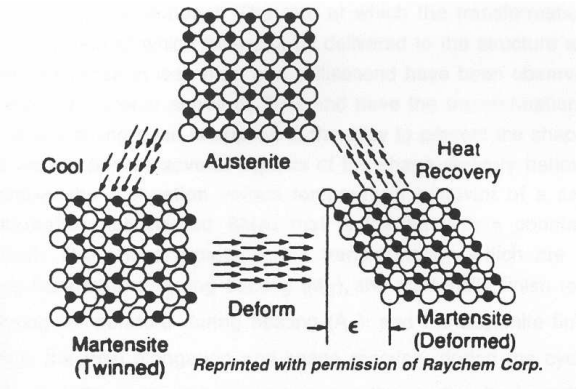

Figure 33: Crystalline states for shape memory alloy (from Hodgson & Brown, 2000)

The 'shape memory effect' is then incorporated through the addition of heat, which allows the material to reverse from the tilted form back to the cubic crystal form. The thermodynamic forces experienced in the phase change are much stronger than the yield strength of the alloy, and therefore predominate over any resistance to crystal restructuring. In addition, the forces needed to de-twin the martensite are significantly less than the yield strength of the austenite, completing the cycle of a heat engine. The material can therefore be deformed in the cooled state with little work expenditure, and the application of heat can restore the unstrained specimen. This corresponds to subplot (f) in the accompanying figure. It portrays the addition of stress beyond the martensite's yield strength, adding strain until the detwinned martensite (DM) has been sufficiently strained, and unloading of the detwinned martensite (Huang, 1998). Coupled with the

last step of thermal strain recovery, this is the proposed operation of the shape memory alloy to be implemented on the HECS wing.

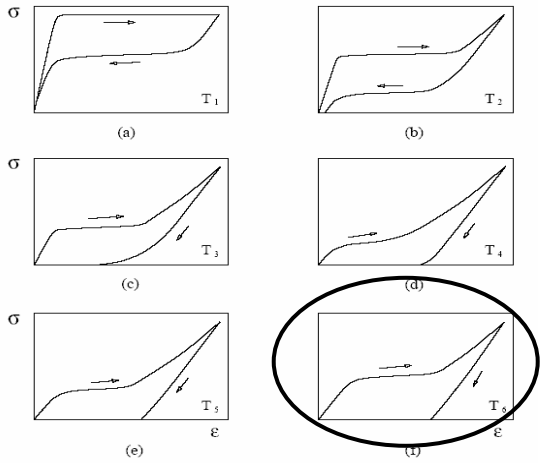

Figure 34: Stress-strain relationships for SMA at various temperatures, $T_1>>T_2>\ldots>T_6$ (from Huang, 1998). Subplot (f) denotes application to HECS wing.

Were the material temperature to be above the TTR before the addition of stress, the 'superelastic' effect of shape memory alloy would be encountered, similar to subplot (a), wherein the material would accept strain with no additional stress beyond the yield strength of the austenite, but upon unloading would immediately revert back to the zero-strain, ordered cubic structure of the heated austenite.

4.2 SMA Experimentation – Feasibility of a Materials-Based Locking System

The austenitic SMA wire is configured such that it will be able to carry the loads sufficient to overcome the aerodynamic forces and allow the wing to furl its shape. It has a high yield strength before deformation – on the order of 25-100 ksi (Brown et al, 2000), though this is highly nonlinear with temperature. However, a key problem with the SMA system is that the wires are forced to carry the loads regardless of state. The wiring has now become a principal load-bearing structural member, in addition to serving as the actuator for the system. This means that while the wing structure may be able to retain the furled shape in the heated austenitic state, it must also be able to do so in the passive

martensitic state without constant power consumption. Many mechanical devices have already been designed to account for this drawback of SMA, including stops, locks, and other potential energy barriers to overcome to avoid allowing for the detwinning of the martensite. It would be favorable from both an energy or weight perspective to try to utilize the structural properties of the martensitic SMA itself, rather than resorting to other mechanical locking devices.

The thermo-mechanical properties of shape memory wire vary based on the composition of martensite and austenite, and various models have been proposed for determining them at particular temperature/phase/stress states. However, for practical purposes, the published values for Young's Modulus E and yield strength σ_Y in the martensitic and austenitic states are sufficient. Dynalloy's quoted maximum pull force of 4.4 lb-f for the wire diameter used, indicating the yield strength of austenite given the published diameter wire, is 25 ksi (Brown, 2000). The published yield strength of the martensite is 10-20 ksi before tripping to detwinned martensite, with $E_M \approx 4\text{-}6\text{x}10^6$ psi and $E_A \approx 12\text{x}10^6$ psi. Upon tripping to the detwinned form, the martensite will only experience between 0.17% and 0.50% strain in the twinned state, and then easily transition to much higher strain rates. A stress-strain plot of an antagonistic wire pair is shown below.

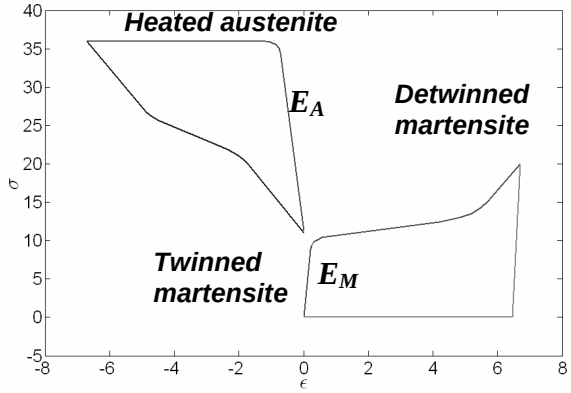

Figure 35: Stress-strain plot for antagonistic SMA showing relative stresses and achievable deformations. Wire is preloaded from external force on wire to be heated.

More importantly, it will only allow for between 1.75 and 3.5 lb-f allowable force to be applied to any of the cooled tendons before they will deform plastically. Once this happens in a parallel bay of wiring with any uneven loading, a tendon will experience a non-reversible plastic deformation, and will not be subject to the same stresses as the other wires until all have been equally deformed. This means that enough vibration or rotation due to flexure about any axis other than the intended joint axis will cause a chain reaction weakening the twinned martensite one strand at a time, until all parallel strands have been tripped to the detwinned martensite and the structure has deformed to the planar state or even hyperextended to a dihedral shape. There are four solutions to this problem:

1. Include many more wires than are necessary to achieve the furl maneuver, in order to try to avoid having any particular wire reach plastic deformation. For this to work, additional power is required to heat all parallel wires, with an added problem of not allowing aerodynamic forces to restore the furled wing back to the planar shape when cooled without full antagonistic operation.
2. Incorporate some form of locking system that allows for rigidity when necessary, but can become compliant when shape change actuation is desired.
3. Fabricate the structure with high precision to allow for a slight increase in number of wires such that the passive, twinned martensite might also be able to carry the aerodynamic load in the furled state. This is impractical in initial prototypes due to flexure of the wing under compressive loading and twist due to aerodynamic loading, and would still require additional restorative forces to regain the planar wing shape.
4. Send continuous power to the wires in order to hold them in place.

Initially, the fourth option of keeping the wires continuously heated will be selected to facilitate fabrication and keep weight requirements down at the expense of energy

consumption. The smart skin will serve as the second option, and holds promise for vast energy reductions with only a slight weight increase.

4.3 SMA Model

Various models have been proposed for shape memory alloys, many of which relevant to the materials community to describe microscopic shape change as a function of a coarse grain model. This has taken both one-dimensional and three-dimensional forms, representing phase (austenite, detwinned martensite, and twinned martensite) as a function of various parameters. For the purposes of implementation on a mechanical system, a model needs to be developed for the HECS wing application which takes into account the power input into the system and outputs mechanical strain, for use in a feedback control law. This can be based on both constitutive laws and analytical models.

The basic relation between power input and temperature can be expressed with a general heat transfer model. The rate of heat input into the wire can be expressed as the resistive heat added less the convective heat to the environment. Conduction losses are assumed to be negligible compared to the convection to the air, as very little of the wire is in contact with other conducting surfaces. The model is then:

$$mc_p \frac{dT}{dt} = \frac{V(t)^2}{R} - hA_C\left(T - T_\infty\right) \tag{22}$$

where m is the mass, c_p the specific heat, T the temperature, V the time-varying voltage, R the resistance, h the convection coefficient, and A_c the surface area of the wire. This version was also used in rotary shape memory actuator devices (Elahinia et al, 2004), and a comparable nondimensional version is used by Huang in his doctoral thesis on SMA, validating the conduction-free model. The convection coefficient assumes an average value of 35 W/m^2-K (Vitiello et al, 2004), and the resistance is assumed to be an average value between the heated and cooled states. From this, a model of the temperature can be

fit to one of the analytical models of the wire, developed by Liang and modified from a rate model by integration:

$$\begin{aligned} &\sigma - \sigma_0 = E(\varepsilon - \varepsilon_0) + \theta(T - T_0) + \Omega(\xi - \xi_0) \\ &\xi^{M\to A} = \frac{\xi_0}{2}\cos\left[\frac{\pi}{A_f^{'} - A_s^{'}}\left(T - A_s^{'} - \frac{\sigma}{C_A}\right)\right] + \frac{\xi_0}{2}, \\ &C_A\left(T - A_f^{'}\right) < \sigma < C_A\left(T - A_s^{'}\right) \end{aligned} \tag{23}$$

where C_A is defined as the slope of the stress-temperature curve for austenitic SMA, A_s' and A_f' are the start and finish temperatures, ξ is the martensitic fraction, θ is the thermal stress tensor, and Ω is the phase stress tensor (Liang and Rogers, 1990). Based on the findings of Tanaka (1993) and Troisfontaine (1999) for various SMA wire gauges, the transformation temperature range A_f'-A_s' is estimated at 18.8 ^{o}C. Tanaka also calculates the stress/temperature slope C_A at 1280 psi/^{o}C. Based on the low thermal expansion properties (0.2% elongation strain for a 200^{o}C change, compared with 7% contraction strain during phase change) of the Flexinol®, Huang removes the thermal stress term and reduces the system to a relationship between stress, strain, and phase. In the HECS wing mechanism, the stress experienced by the wire is approximately constant – the aerodynamic loading on each segment will remain similar regardless of orientation, only the lift experienced by the wing will change drastically. If wing weight is neglected, and consequently all forces acting on the wing remain constant regardless of orientation, the change in stress can be assumed to be zero. As well, the wire in the cooled state is assumed to be entirely in the martensite phase. The only modeling difficulty is that the constitutive equation for phase only has a narrow temperature range in which it is valid – below this, it is assumed to be martensitic, and above this, austenitic. Once the wire is all austenite, the maximum strain rate is reached, and further contraction is no longer possible, unlike in reality, where a large temperature variation can still induce small strain changes. The plots below show the difference between the simulation and Huang's earlier experiments.

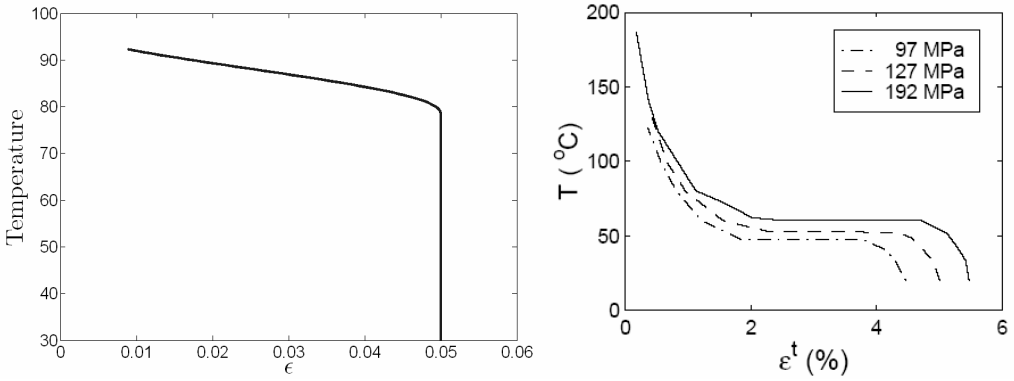

Figure 36: Strain vs. temperature with simple cosine phase model (left, Manzo 2006) compared to model without high temperature simplification (right, Huang 1998). Simple model valid for small strain rates and moderate temperatures

Though the quoted transformation temperature for the SMA is 70°C, the dependence of the transformation on pre-stress raises the actual transformation temperature in the physical system to 78.7°C for observed phase change, although in the model the start and finish temperatures are the initial quoted values. The final model is then:

$$0 = E(\Delta\varepsilon) + \Omega\left(\frac{\xi_0}{2}\cos\left(T - A_s^{'} - \frac{\sigma}{C_A}\right) - \frac{\xi_0}{2}\right), \qquad \xi = \begin{cases} 0, T < 78.7 \\ 1, T > 97.5 \end{cases} \tag{24}$$

with the temperature defined above in Equation 20, and where the phase cosine model is valid within the specified range only, and binary outside of that range. This range represents the stress-adjusted transformation temperature range, expressing the dependence of the phase on the stress already loaded on the wire. The nonlinear model cannot be simplified further, and is still subject to a simplified model of the thermomechanical region where the temperature is above the stress-adjusted final austenite transformation temperature, as well as any region where contraction is greater than what is needed, requiring passive cooling. A simulation of this system with feedback control is discussed in section 4.4.

4.4 SMA Control Logic

To actuate the SMA network, the coupling between tendons is done electrically as opposed to mechanically like the Da Vinci device. Each tendon bay can be controlled independently, but will be programmed to function in tandem to yield the same proportional shape as the mechanical spools would provide. In this way, infinite variability between segments is available for further testing and demonstration of principles. This was achieved by connecting each individual parallel wire bay with an internal power bus at one end of the wire, and then the other end of each wire bay with a control bus. The SMA wire would then be permanently tied to the high rail of a +12 V power source, and the circuit would be closed by the on-board circuitry as determined by the control logic.

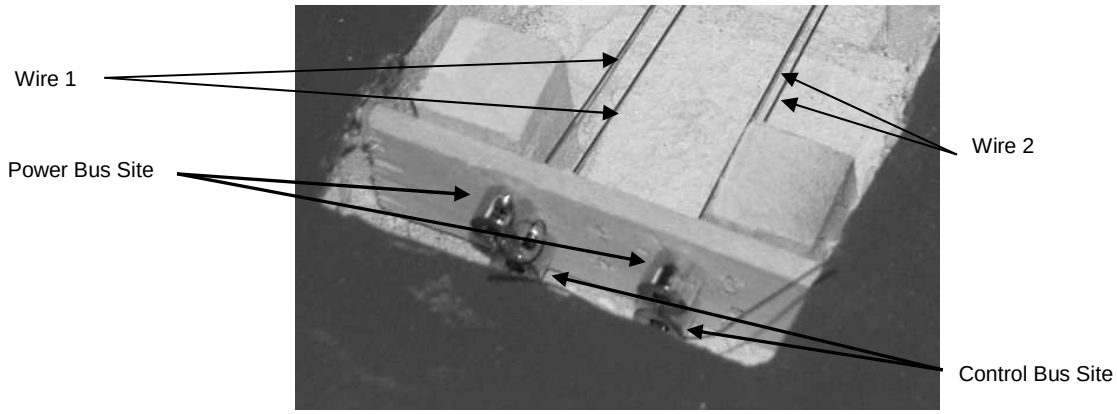

Figure 37: Section 2 SMA wiring configuration

To control the system, the ATMEL mega88 chipset was used in conjunction with the rotary potentiometers placed at the joints in each of the section ends as sensors. The mega88 chip has onboard analog-to-digital conversion, and was therefore able to convert the infinitely variable sensor signal into a 10 bit digital input to the controller. This was deemed sufficient resolution for the first set of testing, but could easily be increased by increasing the maximum voltage of the potentiometers and restricting the operating range to within the 5 volt maximum of the mega88 controller, given rotations on the order of 5-35 degrees.

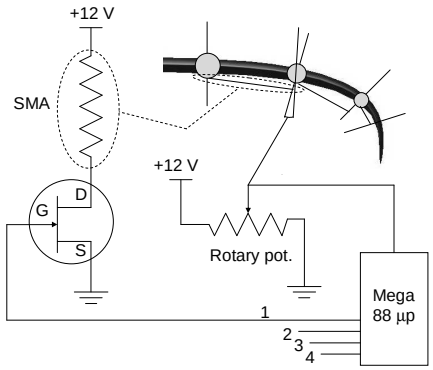

Figure 38: Circuit diagram of HECS wing mechanism

With the sensor inputs into the controller, experimentally determined angular reference points $\theta_{\gamma i}$, where *i* denotes station location, could be programmed in the proper ratios to create the HECS wing's approximated, discretized curvature. This was based on the nominal (flat) setpoint configuration $\theta_{\beta i}$ and the angle proportionalities that have been determined earlier. The potentiometer has a range of $270^o \pm 5^o$ over the 1024 discrete possible ADC outputs, so an approximate conversion between desired angle change and desired digital setpoint values could be determined geometrically. This was instead done experimentally, in order to avoid errors due to potentiometer tolerancing.

The feedback used for the system was a proportional-integral controller that took the angular sensor data as the system output and the desired angular setpoints as the reference signals. This type of control is effective at tracking a reference position with zero steady-state error, and so provides the most accurate means of reaching the desired wing configuration. The speed of the response can be tuned with the gains K_p and T_i, which can control the rise time and ringing in the system. These setpoints could be changed on the fly according to the needs of the aircraft, and were chosen for demonstration purposes to allow for two reference configurations: a planar wing state, where $\theta_{\beta i} = 0^o$ for all *i*, and a furled wing reference state, where the angles were as determined by the discrete wing geometries. Human input allowed for switching between these operating points, as well as operating a kill switch to disconnect all power in case of mechanical failure.

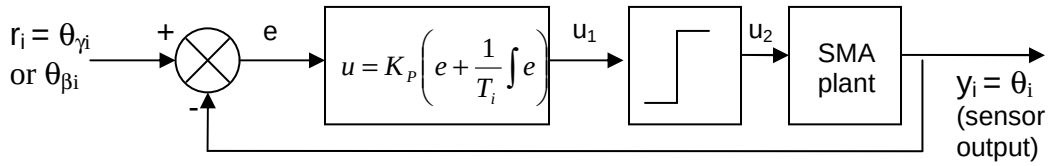

Figure 39: Block diagram for P-I controller used in HECS wing, showing nonlinear saturation/switching logic taking u_1 (linear model) to u_2 (pulse-width-modulated, position saturation) control levels

This controller is nonlinear in three respects. First, the SMA does not heat immediately, and has its own thermally-influenced dynamics that are affected by local temperature, cooling sources, aerodynamic loading, and various other nonlinear effects. Second, the wire can be heated with the controller, but it cannot be cooled. This must be done through convection, which is out of the scope of control of the system. Because of this, the controller switches off when the desired setpoint is reached, such that during overshoot the system disables the feedback controller until cooling and restorative aerodynamic forces bring the wing within the controllable range. Third, the control signal is pulse-width-modulated, and therefore does not send a continuously varying voltage signal but rather an on-off switching logic from a fixed voltage supply. The perceived voltage on the wire is variable based on fast switching rates (1 kHz and higher), but the controller is still effectively binary. It is only within a localized range just below the desired angular setpoint that the controller/SMA wire network functions as a roughly linear system, though the controller is very effective at quickly reaching and maintaining the correct angular position regardless of this nonlinearity.

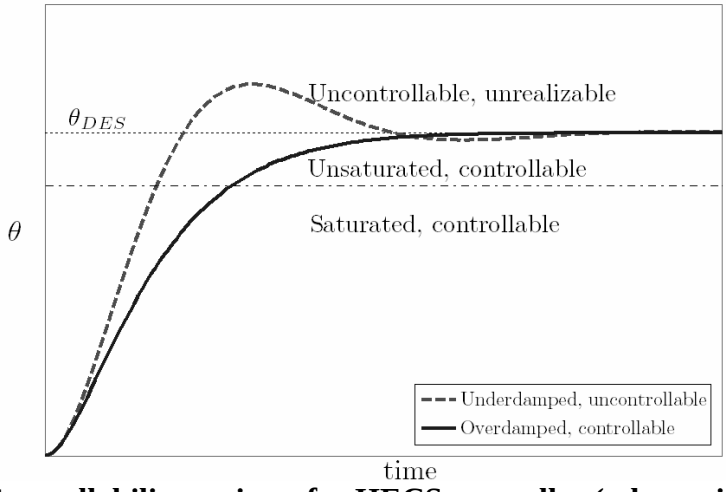

Figure 40: Controllability regimes for HECS controller (schematic only). The system must allow for passive cooling before control resumes, and therefore cannot behave linearly for systems with overshoot

The closed loop system, which consists of the system of equations in section 4.3 and the P-I controller above, was simulated using MATLAB. An optimal integrator gain was chosen to allow actuation of the second joint within 1 second with reasonable amounts of overshoot and ringing. The power to the system is restricted based on position overshoot, so the voltage history shows the system reaching its desired angle setpoint and then shutting off, allowing the wire to cool before reheating. This voltage also is programmed to saturate at a point that yields the maximum recommended current of 2.75 A for this wire gauge as based on the resistance. The power input for the system mimics that used in the experiment, where a circuit pulses power of a certain maximum voltage by varying the duty cycle every 1 ms and can be limited based on the wire's current-carrying capacities. The end result in simulation is an average voltage of .07 V once the wire reaches the desired strain rate, or a duty cycle of approximately 2%, to sustain the required proportion of austenite, around 18%. The temperature behaves as a second-order system, due to the dependence on the square of the voltage which experiences a ramp input. The strain, phase, and angle data is valid predominantly in the stress-adjusted temperature range bounded by the equations and depicted graphically on the temperature plot, above and below which the wire is 100% of either phase and at

maximum contraction/elongation. However, as the temperature reaches this range within 0.4 seconds and does not deviate outside for the desired reference signal, the model is valid.

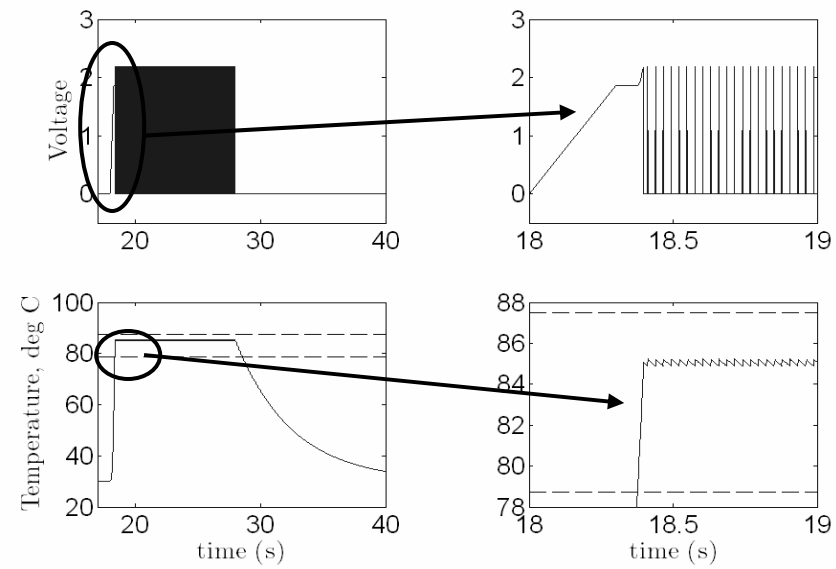

Figure 41: Time history response of voltage (top) and temperature (bottom) for HECS wing joint 2

The system is able to respond quickly to a step input from θ=0 to θ_{ref}, and can track this desired reference signal with minimal steady-state error by using the linear proportional-integral feedback controller despite the inherent nonlinearity of the system. The strain, phase state, and corresponding θ_{rel} all indicate this nonlinearity in their sawtooth-like response, where the wire reverts to a higher martensitic phase proportion during cooling until the power input is reengaged by the feedback saturation logic. This sawtooth is sharper at the leading edge and shallow on the downward slope, as the system cools slower than it can be heated by the stagnant air that is partially insulated by the foam around it.

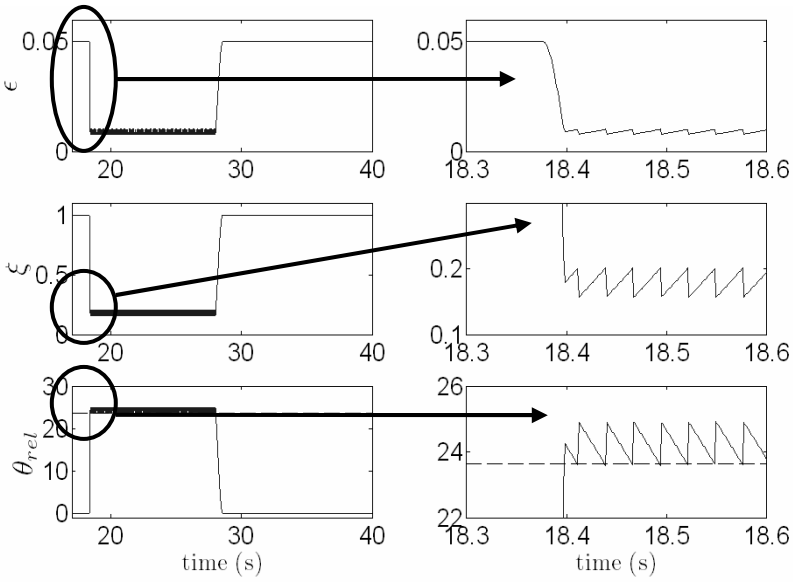

Figure 42: Time history response for strain (top), martensite fraction (middle), and relative angle (bottom) for HECS wing joint 2

One further confirmation that the simulation parameters are valid is that the system has a cooling time of approximately 12-15 seconds before reaching ambient temperature, which agrees well with the factory quote of 13 seconds required for cooling between cycles (Brown, 2000).

4.5 Overall System Capacity

The end result of this type of control is a system that can be configured not only to the planar and furled HECS wing shapes, but to any of the intermediate configurations within the resolution of the ADC on the microprocessor, or to any arbitrary shape within the bounds of the SMA. This can all be controlled by changing the referential setpoints of the feedback control law, and then set to switch between a number of modes, given desired flight characteristics. If only the tips were desired to deflect, for example, then the reference points at the root could remain at the nominal planar configuration, and a wing could be formed with a structure more resembling a straight wing with endplates. The limitations of the SMA are determined by the factory specifications for the desired lifespan of the wire – a transformation strain of 8% is the maximum, but for 100 cycles it

reduces to 6%, and 4% for 100,000 cycles. This 4% contraction satisfies the length conditions for the wires used in all but one section where it requires 5% of the total wire length used to attain the desired HECS wing curvature, but it will be sufficient for testing purposes. The resulting workspace can be seen below; it represents the range of motion of the current configuration of the SMA wire, which is oriented such that the strained martensitic configuration is the planar wing shape, and the contracted wire yields the furled shape.

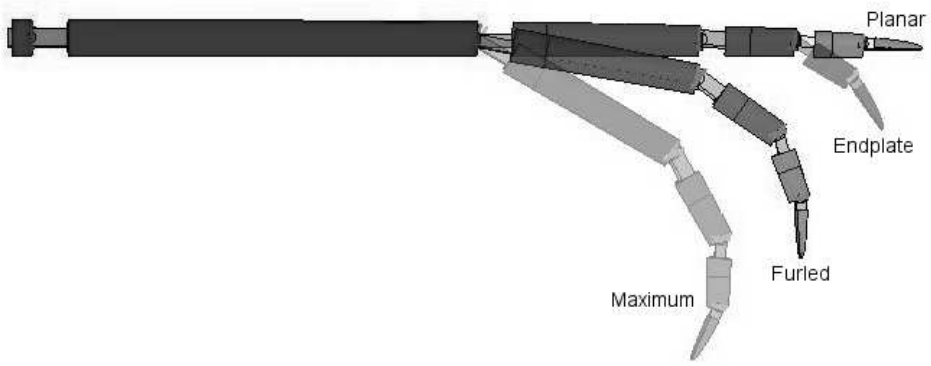

Figure 43: Current workspace of HECS wing mechanism-SMA actuator pair.

If the wing shape was desired to take on a wave shape or curve in the opposite direction, the strained configuration of the wire could be set at a higher angle such that there was a positive dihedral on the wing before contracting the SMA. This would have to be done physically before construction, rather than electronically, but would yield the same workspace range, rotated to the user's specified configuration.

Chapter 5: Experimental Results

5.1 Wind Tunnel Setup

The finished morphing wing was tested in the Cornell low-speed wind tunnel and run at a speed sufficient to sustain the planar wing shape, in a range of 40-50 mph. Below this, the tip section weight was greater than the tip lift, and the wing lifted at the root but sagged at the tips. This problem resulted in an increase in the amount of work that must be done by the shape memory wire in the proximal bays in order to overcome the lift forces generated by windspeeds high enough to lift the wingtips, which resulted in overstraining those wire bays. Initial predictions made in section 3.3.1 on necessary wire force proved insufficient to overcome the combination of aerodynamic forces, friction, and resistance from the pre-strained skin mechanism. Because of this, the amount of wire had to be increased by up to 50% in the third section in order to account for the higher loading. With this modification, the wing was both able to sustain a 'furled' shape under loading and hold in a planar state with the SMA cooled. Various setpoints were chosen to approximate the furled shape, with a conservative estimate of the shape approximation chosen to preserve the life of the SMA wire, relative angles being decreased by 5-10% to preserve the life of the SMA wire.

The data was collected in a similar manner to that of the initial quasi-static wind tunnel testing of the rigid HECS wing shapes. The primary difference is that the morphing wing model only consisted of a half-wing, which had to be cantilevered off the force balance in order to achieve the largest operating range for the forces and moments. The JR3 6-axis load cell is capable of measuring up to 5 lb-f in the radial axes, 10 lb-f along the axis of symmetry of the load cell, and up to 20 in-lbf of torque in two of the three moment directions. This means that, in order to measure lift forces on the order of 5-10 lb-f, the

wing had to be mounted parallel to the plane of the force balance, rather than protruding directly outward, where lift acts as a radial force. To this end, a simple mounting joint was fabricated which rigidly attached the two dowels from the wing to a rotating joint mounted above the sting via a small aluminum block, all separated from the wing and the airstream by a splitter plate. The practical limits of the force balance were nearly reached in all configurations, such that the test apparatus needed to be zeroed with a known mass suspended to counteract the x-moment generated by the large cantilevered wing experiencing zero lift. This mass was removed when the proper amount of lift was generated by the fans, which is accounted for during post-processing calculations, such that the force balance is not in saturation.

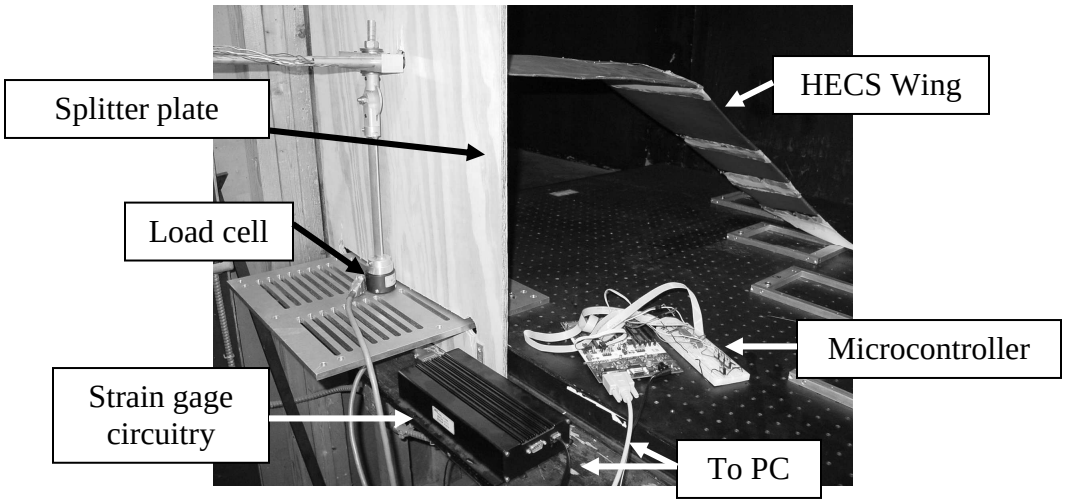

Figure 44: Dynamic wind tunnel test setup

The data collection system consisted of a MATLAB-based graphical user interface, in conjunction with the serial output of the SMA microcontroller. This system was able to log the angular sensor data at up to 20 Hz, and aerodynamic data from the six degrees of freedom at upwards of 50 Hz. As well, a selectable pre-processing low-pass filter cuts signals above 100 Hz to reduce noise from vibration. For the purposes of this test, the aerodynamic data was collected at 50 Hz and averaged every 0.05 seconds, to be certain that no information was lost while logging both aerodynamic and angular information at

approximately the same frequency. This data, however, consisted of raw forces and moments, and required post-processing in order to obtain key information about the planar, furled, and morphing wing.

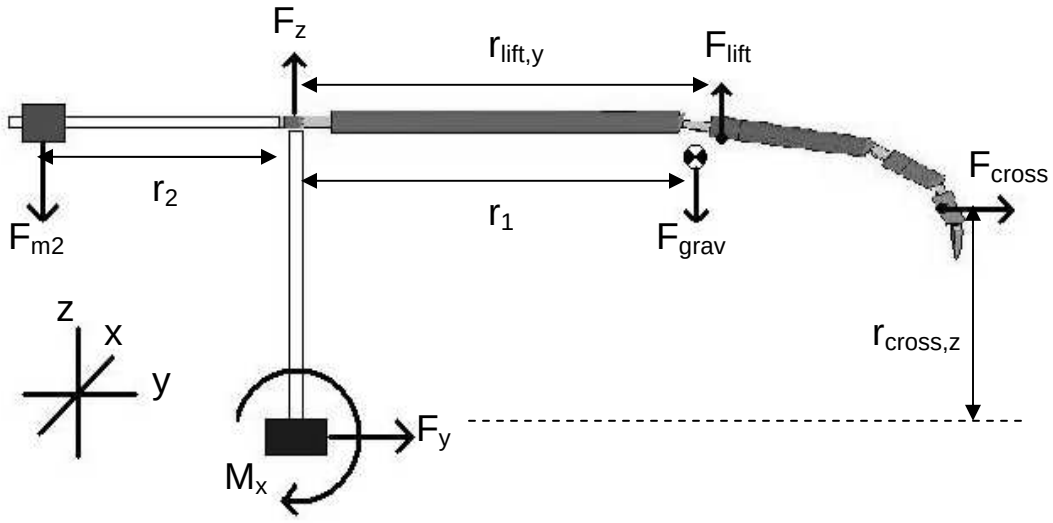

Figure 45: Force balance in the Y-Z plane

The forces and moments could be related by the geometries of the wing, which become more complicated when furled due to spanwise forces. In the x-z plane, (all orientations described in terms of force balance orientation, not true aerodynamic direction) the forces and moments can be related to the force balance forces and moment F_z, F_x, and M_y by:

$$\begin{aligned} F_Z &= m_2 g + F_{Lift} \\ M_X &= m_1 g \Delta r_1 + m_2 g r_2 - F_{Lift} r_{Lift,Y} - F_{Cross} r_{Cross,Z} \end{aligned}, \qquad (25)$$

where Δr_1 represents the change in C.G. location due to wing shape change. While zeroed with no lift forces, it is assumed that the wing shape is roughly that of the furled wing, such that during the morph, the quantity $m_1 g \Delta r_1 = 0$, and while planar, the C.G. shifts approximately 0.25" in the +y direction. This information, then, can be used to find not only the lift on the wing, but the location along the span at which the lift force acts, $r_{Lift,Y}$.

The equation for drag is simple, as the addition or removal of calibration weight m_2 does not affect the x-y plane:

$$\begin{aligned} F_X &= -Drag \\ M_Z &= -Drag * r_{Drag,y} \end{aligned} . \tag{26}$$

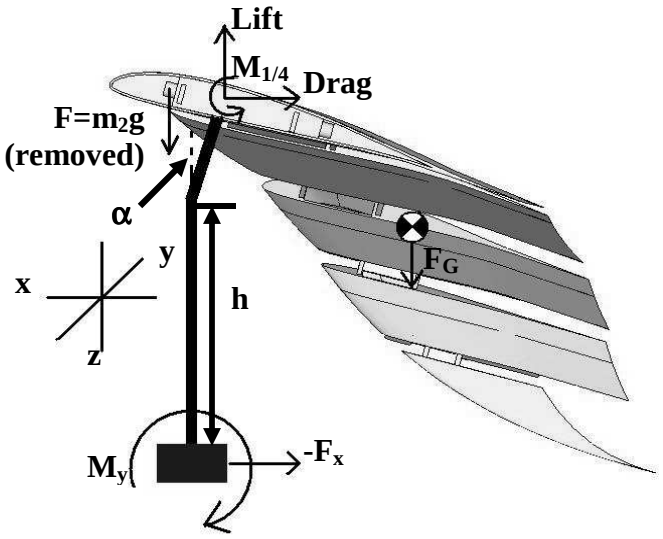

Figure 46: Force balance in the X-Z plane

In the y-z plane, the moment about the quarter-chord point can be determined based on the rotation of the wing about the sting. This can be accomplished by using a coordinate transformation in three steps: translation of the sting rotation point to the origin, rotation about this point by α, and translation back to the true position. The resulting moment arms are then determined by this geometry.

$$\begin{bmatrix} -r_{x,new} \\ -r_{z,new} \\ 0 \end{bmatrix} = \begin{bmatrix} 1 & 0 & 0 \\ 0 & 1 & h \\ 0 & 0 & 1 \end{bmatrix} \begin{bmatrix} \cos(\alpha) & -\sin(\alpha) & 0 \\ \sin(\alpha) & \cos(\alpha) & 0 \\ 0 & 0 & 1 \end{bmatrix} \begin{bmatrix} 1 & 0 & 0 \\ 0 & 1 & -h \\ 0 & 0 & 1 \end{bmatrix} \begin{bmatrix} -r_{x,old} \\ -r_{z,old} \\ 0 \end{bmatrix}. \tag{27}$$

$$M_{1/4} = M_y - F_{Drag} * r_{Drag,z} - F_{Lift} * r_{Lift,x} + m_2 g * r_{m_2,x}$$

The weight of the wing is removed from the moment by zeroing before data is collected, but as the weight m_2 is removed during speed ramp-up, the contribution from mass m_2 must be added to the moment. This is used to form a basic force/moment translation from the sensor to the quarter-chord point, and makes no additional assumptions about the actual location of lift and drag on the wing, which are impossible to measure without

additional sensors. However, the moment about the quarter-chord point at the root, which is assumed to be the center of pressure, is a good measure of the stability of the wing before tail contributions are added.

5.2 Quasi-static Aerodynamic Comparison Against Smooth Wing

The final results showed similar results to those found for the continuous wing testing. The lift coefficient for α=0^o varied from 0.022 to 0.0205 from flat to furled, or a drop of 6.7%. The drag increased by 2.1%, and the moment decreased by 12.1%. The quasi-static smooth wing tests projected a decrease in lift coefficient of 13.6% at this angle, though it also predicted a decrease in drag. However, the variance in both the smooth wing and morphing wing is very high, due to the sensitivity range of the load cell, as well as the relatively low drag values at these lows speeds, making the signal-to-noise ratio very high. The practical range of α that could be tested ranged from -2^o to 11^o due to the sensitivity of the testing equipment in the presence of excessive vibrations or high wing loading. At too low an angle of attack, the wind speed needed to be increased drastically to create sufficient lift to raise the wing, creating large force and moment fluctuations seen by the load cell, whereas overly high angles of attack generated much more lift on the root section before the tip was raised, again saturating the load cell. Overall, a similar trend was shown for the discretized wing as was seen for the flat wing in the tested range. The lift forces were the most consistent quantities measured, and did follow a fairly linear trend until rolloff around α=10^o. An offset of approximately 0.15 in lift coefficient can be explained partially by different angle measurement conventions and partially by losses in lift due to tip sag, twist, and gaps not generating the full amount of lift when compared to a continuous wing. The drag, however, was quite comparable, which is an indication that the discrete model's skin system did a fair job of maximizing lift and minimizing parasitic drag by creating an airflow boundary between upper and lower airfoil surfaces.

At α=10^o, the system is at a configuration that saturates the load cell when the wind tunnel is run in any of its fixed speed ranges, and is only valid in the z-direction (lift).

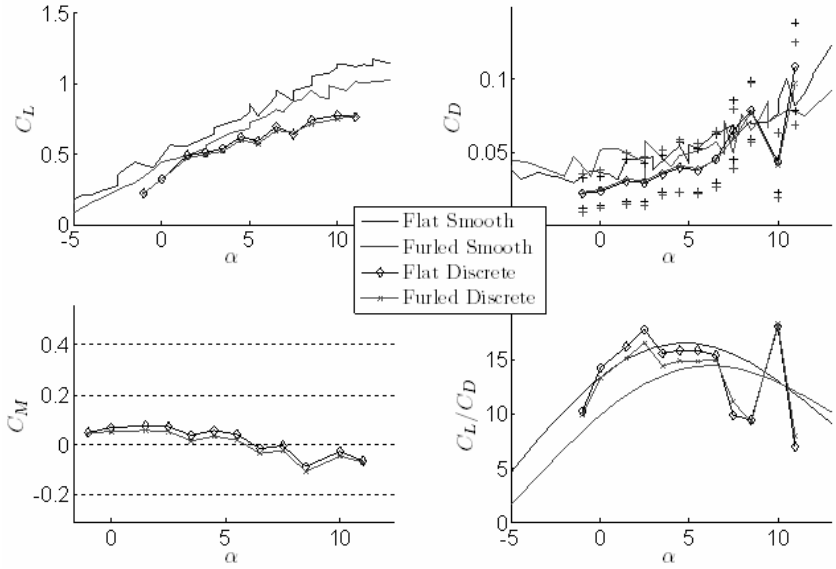

Figure 47: Aerodynamic coefficients for planar and furled HECS wing, smooth (polynomial fit) and discrete

5.3 Furled vs. Planar Results

The aerodynamic forces in the planar and furled states can be measured for the steady-state case once the geometry change has been accounted for in post-processing (shift in C.G., change in moment arms for lift and drag when $\alpha \neq 0$, etc). During the morph, the wing was sent the command signal to furl for at least 10 seconds, to allow for sufficient data to be sampled once the wing had achieved the fully furled state. The unfiltered results, which reflect a 2-state geometry model (flat or furled, transient results ignored), show a distinct change in the lift on the wing between planar and furled shapes, as well as a distinct location shift in the center of lift and drag. Both the center of lift and center of drag shift closer to the root of the wing, though the drag shifts much closer to the root of the wing than the lift, which is still centered at approximately 19” from the root of the 36.4” span. The actual drag does not change significantly, as the frontal projected area does not change during morph.

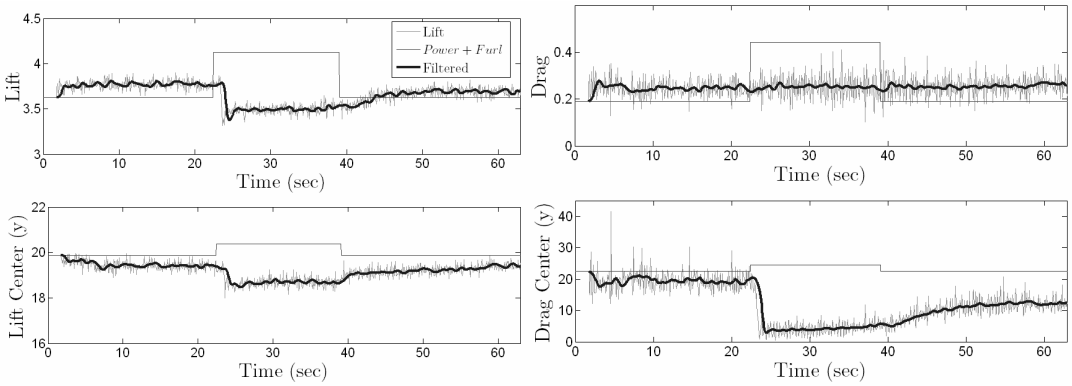

Figure 48: Lift and drag variation in morphed state

The drag on the wing does not have a high signal-to-noise ratio, and therefore measurement is much more affected by vibration than lift force. However, in all tests, the drag center moves inboard by approximately 15", reflecting a change of around 80%. A change this significant could indicate not just that the wingtips were affecting the drag and furling them inwards would move the drag center closer to the root, but also that the aerodynamic effects of the morphing shape are to blame for the change in drag.

Over a range of α, trends were fairly consistent with theory as well as continuous wing testing. Given that the planar wing was very difficult to fully extend given low tip lift forces coupled with high weight, it makes sense that planar lift coefficient is typically around 4% higher than the furled lift, which is a smaller discrepancy than the 14% predicted by theory in chapter 2, or the 10-15% seen by earlier tunnel tests of the continuous wing. One interesting observation that did not occur previously was that the lift at $\alpha = 7.5^{o}$ was consistently higher for the furled wing compared to the flat wing. This was not predicted by earlier testing, though it was hinted at by theoretical explanations of vorticity modification. The result was consistent in all test runs at 7.5^{o}, and does not explain why a drop in lift due to span decrease is not present instead, which is to be expected based on other tested angles.

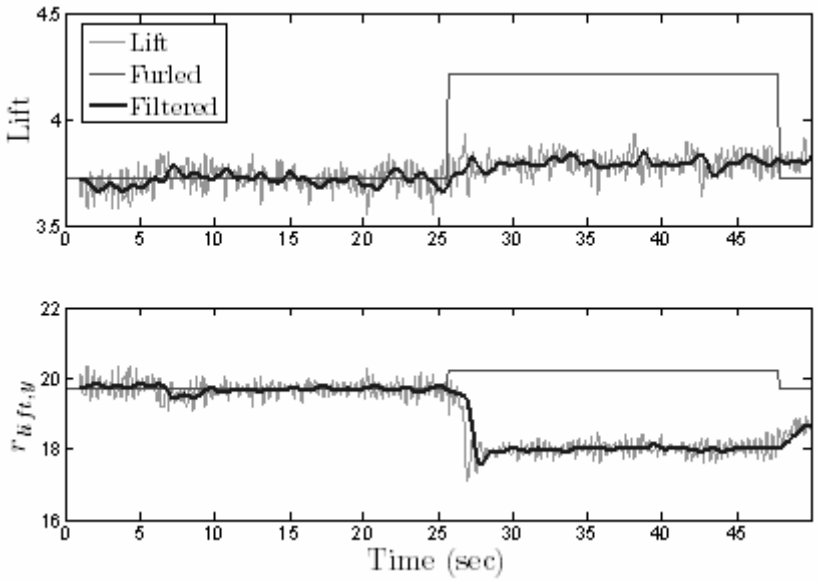

Figure 49: Lift increase and spanwise migration at α=7.5^{o}

This repeatable result is an indication that the vortex wake of the furled HECS wing actually benefits the performance significantly, as the span has decreased 16% and yet the wing is still able to yield an increase in lift. At this angle of attack the wing correlates with the earlier wind tunnel testing conclusion that there is a narrow band at which the furled wing performs better than the planar in overall lift-to-drag ratio. Much of the tip lift is lost during the furl, yet the average lift generated by the proximal sections increases, as can be seen by the proximal lift migration. Defying conventional aerodynamic theory, the furled wing shape is able to generate more lift than the planar wing with only 84% of its total span, and with a smaller planform area. While the results may not prove as promising as the papers by Burkett and Lazos had conjectured, it still validates the nonplanar wing shape as a novel means of lift generation.

5.4 Transient Aerodynamic Results, Morphing Time

In order to analyze the data, a smoothing filter needed to be applied to the raw data to account for the evident sensor errors, as well as a fourth-order Butterworth filter to then further simplify the results. The smoothing filter was of the form:

$$\left|\theta_i - \theta_{i-1}\right| \geq 5 \;\; \left|\theta_i = \frac{\theta_{i-1} + \theta_{i+1}}{2}\right., \tag{28}$$

where angle values represent 8-bit digital sensor data, such that if a point experiences a sensor 'pop', this is replaced by the average of the neighboring points. After applying this smoothing filter, a Butterworth filter was applied with a cutoff frequency of a 0.16 Hz, to eliminate all high-frequency noise. The resulting filtered plot is shown below.

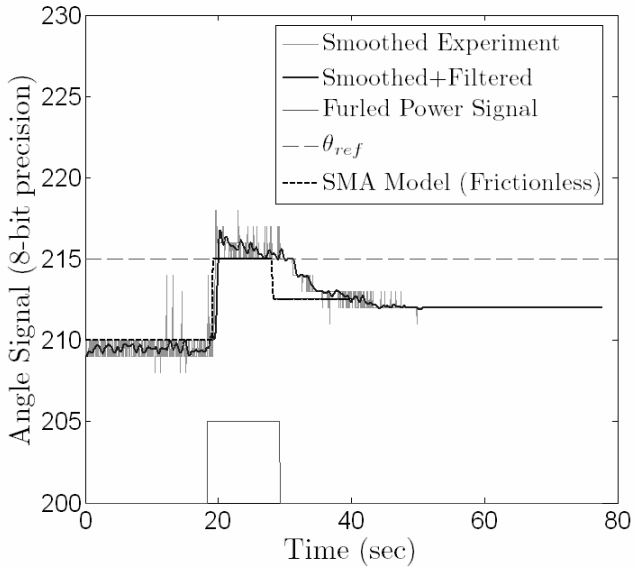

Figure 50: Section 2 time history response of SMA bay showing reference angle, with power signal and SMA model of section 4.4 with no friction and noiseless sensors overlaid

The filtered data shows more clearly the trends for lift and drag centers, but indicates that the lift and drag may experience position overshoot before reaching steady-state value. The results show that, for $\alpha=0^o$, the four joints will all cross their desired setpoint within 1.5 s, and will all settle to these setpoints within 3-3.5 s. This overshoot is slightly more pronounced in the root sections, where more power can safely be sent to the wire bays without risk of damage, consequently causing more overshoot as the wire quickly heats and therefore contracts, reducing the angle before the system can respond. It agrees with the finding that reaching the desired setpoints for the outer two sections takes noticeably longer than the root sections, though the time from first crossing the setpoint and the final settling time is significantly less, as the system behaves as if it is more highly damped

due to lower power signals and smaller wire bays. However, due to the nature of the controller, it cannot behave as a linear system since the power is cut upon reaching the setpoint to prevent excess energy expenditure or risk overheating/-straining the wires any more than necessary. In comparison to the SMA model described in section 4.4, the system demonstrates significantly more overshoot than was predicted, due predominantly to inertia. The model does not take into account accelerating and decelerating the pendulum system in its assumption of constant stress on the actuators – a simplification that limits accuracy for the transient portion of response but will yield adequate results in the steady-state case. As well, the model does not take into account friction. This tends to prevent the wing from raising to the planar state fully upon cooling, and could lead to excessive saturation of the integrator by keeping position error high until overly large contractile forces were developed in the wire to overcome the resistance, causing a sudden surge of contraction on a time scale comparable to the response time of the controller. As well, sensor accuracy as seen by the ADC on the controller could not respond to the sensitivity of the system, causing overly large error readings and again saturating the controller until crossing the desired setpoint.

Chapter 6: Conclusions

6.1 Metric for Success

While the HECS wing morphing mechanism is fully functional, it is difficult to determine if it is a 'good' morphing concept. One of the best evaluation criteria is weight, specifically wing load to wing weight ratio. This metric is used at NASA Langley Research Center. It relates the wing weight per unit area (including control surface hardware) to the wing load value for a fully loaded vehicle in a quantity μ_{GR} (Granda et al, 2005). Different craft fall along different points on the chart, with long range and combat intercept planes such as the Boeing B-47 having high wing loading, light civil planes such as Cessnas falling at the low end of the spectrum, and fighters, STOL, and high altitude craft falling in the middle of the range. Points with wing load to weight ratio lower than 10.5 are deemed weight inefficient. The HECS wing under investigation at Cornell was designed to carry a 15 pound craft while flying at approximately 50 mph. This is reasonable, given the approximate 6.5 pounds of lift per half-wing in the range of 30-45 mph during wind tunnel tests. Even though this model was used in wind tunnel tests only, it is comparable to the design that would be used in an unmanned aerial vehicle, and can be benchmarked as such. The HECS wing used in dynamic testing currently weighs 2.89 pounds for a half-wing, or 5.78 pounds for a full wing with area 4.82 ft^2. This places the HECS wing ratio at μ_{GR} =2.59 for the current configuration, about one fourth of the desired ratio.

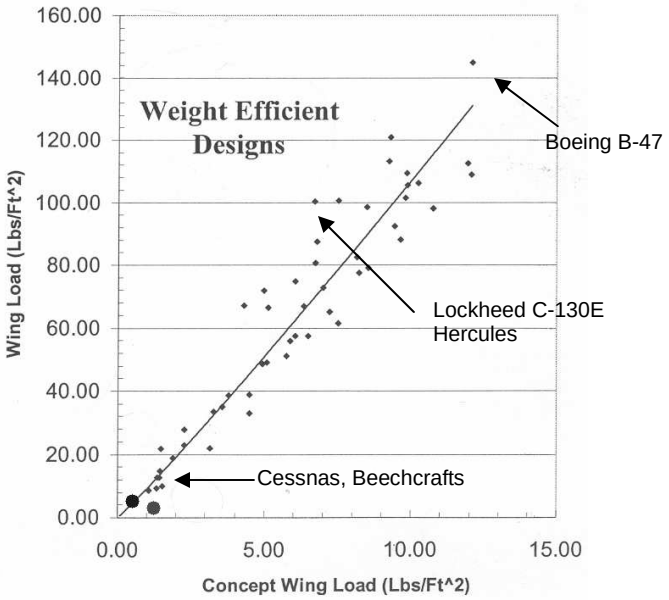

Figure 51: Wing loading vs. concept wing weight (Granda et al, 2005) with HECS data shown. Current configuration in red, refined version in blue.

6.2 Feasibility

In order to approach a more wing efficient design, the weight of the wing mechanism would have to be decreased by at least a factor of 2. A refinement of the skin mechanism and composite structure could allow this. In the wind tunnel design, a wing segment consisted of a solid foam and wood core encased in single-layer fiberglass, which was then filled and painted. With careful construction, a hollow sandwich composite of foam-encapsulated fiberglass airfoils could replace a solid core for weight savings by removing all of the wood and most of the foam. More importantly, different finishing techniques could eliminate the need for a filler material, which accounts for up to 35% of the net wing weight. With improved skin sections eliminating the metal sheaths used for easy skin removal during repair, a further reduction of at least 25% total wing weight could be accomplished, yielding μ_{GR} =6.5. To increase this value above 10.5, the lift on the wing would have to be increased, meaning the mechanism would have to be sized differently in order to account for further compressive loading. Flying the craft at 65 mph at α=0^o, compared to 45 mph in dynamic testing, would increase the lift from 13 to 27 pounds, which is not an unreasonable cruising speed for a 72” span aircraft. In order

to overcome the lift forces, the number of wire bays would need to be increased by a maximum of 50% in each section, increasing net resistance by adding SMA wires in parallel to the original system. This could require a larger power supply, but could also be avoided by decreasing the length of SMA wire in each section to exactly the right amount necessary for 4% contraction. In the end the true HECS curvature could be attained, but this tradeoff would decrease the overall workspace outside of the HECS relative angle setpoints in order to allow for the same power source to be used. This addresses the issue of functional trade-offs; in order to keep weight low, the envelope of morphing must be kept within a certain limit. The structure of the airframe would be able to handle the loading, as determined by the FEA analysis and final factor of safety of greater than 10, meaning this system could scale up to fly at 65 mph on the same span craft, yielding μ_{GR} =11.7. This would meet the NASA LaRC criterion for weight efficiency, allowing the mechanism to move into further stages to determine its functionality in the field.

6.3 Future Work, Modifications

A few additions could be added to make this wing mechanism more attractive. To take advantage of the geometry, a wingtip yaw controller could be added between the 2 most distal wing sections. This would allow rotation of the tip with small SMA actuators in a Stewart platform-like configuration, which would be more efficient and lightweight than linear actuators. This could decrease the size of the rudder needed at the tail, and would drastically increase the yawing moment by controlling the tip vortex shedding off each wing separately. With lightweight SMA actuators replacing servos, this could be a further source of novel weight reduction coupled an ability to generate large control moments.

Additionally, an active rigidity skin could be formed from novel materials such as Cornerstone Research Group's Veriflex® shape memory polymer, which would reduce power consumption by limiting the time that energy must be pumped into the SMA wire to hold the furled shape. If the skin over the gaps could be load-bearing passively, and could be modified to become compliant on demand in order to morph, then a large amount of energy would be conserved. This skin would need to have a low profile and an embedded heat source, both of which are still being addressed in ongoing research and material fabrication techniques.

Future studies would include development of a more complete model to incorporate flutter due to skin vibration, as well as aeroelasticity effects yielding wingtip deflection. These would be conducted in a more controlled testing environment, where Reynolds number could be accurately modified, and knowledge of boundary layer behavior could be understood. This could lead to intuition about the stall characteristics of the wing for high angles of attack in each configuration, possibly indicating another potential advantage of the furl maneuver. Vorticity effects would need to be studied in greater detail to understand conceptually what the effects of morphing are, using alternative testing equipment and facilities. Additionally, as the SMA wires have a stiffness associated with them, the vibration of the structure varies with the tension in these wires, and therefore the system response as a function of wing shape configuration could be measured.

Concluding Remarks

The HECS wing mechanism has been demonstrated as a viable flight-worthy design using lightweight actuators that is infinitely reconfigurable on-the-fly to user setpoints capable of varying lift-to-drag ratio by at least 7%. The planar HECS wing is shown to defy conventional planar vortex wake theory by surpassing an elliptical wing of similar

planform in tunnel testing, representing a more efficient planform shape than the conventionally idealized shape over a wide range of angle of attack. The HECS wing also demonstrates a repeatable increase in net lift during furled morph despite a span decrease over a narrow flight regime, indicating the effectiveness of varying the vortex wake by the physical constraint of a downward-pointing in addition to the aerodynamic effect of swept wingtips. Further iterations could reduce wing weight to less than 10% of gross take-off weight, making it weight efficient by NASA LaRC's criterion. Consequently, despite all simplifications and minor deviations from the initial proposed design, this final mechanism is a valid reflection on the potential of the morphing aircraft program to expand flight regimes without sacrificing current capabilities.

REFERENCES

1. Abdulrahim, M. & Lind, R. "Flight Testing and Response Characteristics of a Variable Gull-Wing Morphing Aircraft." AIAA Paper 2004-5113, AIAA Guidance, Navigation, and Control Conference Exhibit, Aug. 16-19, 2004, Providence, Rhode Island.

2. Allen, Howard G. Analysis and Design of Structural Sandwich Panels. Oxford: Pergamon Press, 1969.

3. Avallone, E. & Baumeister, T. Marks' Standard Handbook for Mechanical Engineers, 10th Ed. New York: McGraw-Hill, 1996.

4. Burkett, C. W., "Reduction in Induced Drag by the Use of Aft Swept Wing Tips," *Aeronautical Journal* 93 (1989): 400-405.

5. Cone, C. D., "The Theory of Induced Lift and Minimum Induced Drag on Non-Planar Lifting Systems," NASA TR-R-139, 1962.

6. Davidson, J., Chwalowski, P., & Lazos, B. "Flight Dynamic Simulation Assessment of a Morphable Hyper-Elliptic Cambered Span Winged Configuration." AIAA Paper 2003-5301. AIAA Atmospheric Flight Mechanics Conference and Exhibit, Austin, Texas, Aug. 11-14, 2003.

7. Day, Dwayne. "Variable-Sweep Wings." U.S. Centennial of Flight. NASA. 12 Apr. 2006. <http://www.centennialofflight.gov/essay_cat/6.htm>.

8. Elahinia, M., Ahmadian, M., & Ashrafiuon, H. "Design of a Kalman filter for rotary shape memory alloy actuators." *Smart Mater. Struct.* 13 (2004): 691-697.

9. Faulhaber. "Brushless DC-Servomotors: Series 3056 B." 2005. Faulhaber, Inc. Motor datasheet. 27 Apr. 2006. < http://www.faulhaber-group.com/uploadpk/e_3056B_MIN.pdf>.

10. Granda, J., Sandoval, D, & Horta, L. "Morphing Structural Concepts Evaluation Criteria Using Dimensionless Analysis and Computer Simulation". AIAA Paper 2005-2111, 46th AIAA/ASME/ASCE/AHS/ASC Structures, Structural Dynamics and Materials Conference , Austin, Texas, Apr. 18-21, 2005.

11. Green, D., Winandy, J., & Kretschmann, D. "Mechanical Properties of Wood." Wood handbook – Wood as an engineering material. Madison: Forest Products Laboratory, 1999. 4.1-4.41.

12. Hodgson, D. & Brown, J. Using Nitinol Alloys. San Jose: Shape Memory Applications, Inc., 2000.

13. Huang, W. Shape Memory Alloys and their Application to Actuators for Deployable Structures. Diss. University of Cambridge, 1998.

14. Hughes, P., Sincarsin, W., & Carroll, K. " 'Trussarm' – A Variable-Geometry-Truss Manipulator." Proceedings of the First Joint U.S./Japan Conference on Adaptive Structures. Ed. Ben K. Wada, James L. Fanson, and Koryo Miura. Lancaster: Technomic Publishing Company, Inc., 1991. 715-725.

14. Istituto e Museo di Storia della Scienza & The Science Museum. "Leonardo's Robot." Florence, Italy & The Science Museum, London. Museum excerpt. 27 Apr. 2006. <http://www.z-kat.com/company/adv_research/leonardo.shtml>.

15. Lazos, B. "Biologically Inspired Fixed-Wing Configuration Studies." *J. Aircraft* 42.5 (2005) 0021-8669: 1089-1098.

16. Liang, C. and Rogers, C. A. "One-dimensional thermomechanical constitutive relations for shape memory materials." *J. Intell. Mater. Syst. Struct.* 1 (1990): 207-234.

17. Manzo, J., Garcia, E., & Horner, G. "Adaptive structural systems and compliant skin technology of morphing aircraft structures," Proceedings of Smart Structures and Materials 2004: Smart Structures and Integrated Systems. Ed. Alison B. Flatau. SPIE Press, 2004. 225-234.

18. Maughmer, Mark. "About Winglets," *Soaring Magazine*, June 2002.

19. Multhopp, H. "The Calculation of Lift Distribution of Wings". *Luftf. – Forschg* 15 (1938): 153-.

20. Munk, M. M., "The Minimum Induced Drag of Airfoils," NACA Report 121, 1921.

21. Pistolesi, E., "Considerations Respecting the Mutual Influence of Systems of Airfoils," *Collected Lectures of the 1937 Principal Meeting of the Lilienthal Society*, Berlin, 1937.

22. Raymer, Daniel P. Aircraft Design: A Conceptual Approach: 3rd ed. Reston: AIAA, Inc., 1999.

23. Sanders, B., Crowe, R. and Garcia, E., "Defense Advanced Research Projects Agency - Smart Materials and Structures," *J. Int. Mat. Syst. Struct.* 15 (2004): 227-233.

24. Schrenk, O., "A Simple Approximation Method for Obtaining the Spanwise Lift Distribution," NACA TM-948, 1940.

25. Shackelford, James. Materials Science for Engineers: Fifth Edition. Upper Saddle River: Prentice Hall, 2000.

26. Shevell, Richard M. Fundamentals of Flight. Englewood Cliffs: Prentice-Hall, Inc., 1983.

27. Taddei, M. & Zanon, E. Leonardo's Machines: Secrets and Inventions in the Da Vinci Codices. Florence: Giunti Editore S.p.A., 2005.

28. Tanaka, Y. "Transformation start lines in TiNi and Fe-based shape memory alloys after incomplete transformations induced by mechanical and/or thermal loads." *Mechanics of Materials* 19 (1995): 271-280.

29. Tani, J. & Ueda, H. "Active Vibration Control of a Free-Free Beam by Using a Tendon Mechanism." Proceedings of the First Joint U.S./Japan Conference on Adaptive Structures. Ed. Ben K. Wada, James L. Fanson, and Koryo Miura. Lancaster: Technomic Publishing Company, Inc., 1991. 855-864.

30. Troisfontaine, N., Bidaud, P. & Larnicol, M. "Optimal design of micro-actuators based on SMA wires." *Smart Mater. Struct.* 8 (1999): 197-203.

31. Van Dam, C. P. "Induced-Drag Characteristics of Crescent-Moon-Shaped Wings." *J. Aircraft* 24.2 (1987): 115-119.

32. Vitiello, A., Giorleo, G., & Morace, R. E. "Analysis of thermomechanical behaviour of Nitinol wires with high strain rates." *Smart Mater. Struct.* 14 (2005): 215-221.

33. Weissinger, J., "The Lift Distribution of Swept-back Wings," NACA TM-1120, 1947.

34. Wickenheiser, A. & Garcia, E. "Aerodynamic Modeling of Morphing Wings Using an Extended Lifting-Line Analysis." *J. Aircraft*. Unpublished.

35. Wiggins, L. D., et al. "A Design and Analysis of a Morphing Hyper-Elliptic Cambered Span (HECS) Wing." AIAA Paper 2004-1885, 45th AIAA/ASME/ASCE/AHS/ASC Structures, Structural Dynamics and Materials Conference, Palm Springs, California, Apr. 19-22, 2004.

36. Yoshia, K. & Imanaga, K. "Control of Position and Bending-Torsion-Coupled Vibration of Rotating Elastic Plate Using Double Tendon Mechanisms." Proceedings of the First Joint U.S./Japan Conference on Adaptive Structures. Ed. Ben K. Wada, James L. Fanson, and Koryo Miura. Lancaster: Technomic Publishing Company, Inc., 1991. 645-659.